

HOT SUBLUMINOUS STARS FROM THE SLOAN DIGITAL SKY SURVEY: SEARCH FOR RADIAL VELOCITY VARIABLES

Bachelorarbeit aus der Physik

Vorgelegt von

Philipp Jeßberger

04. Januar 2023

Dr. Karl Remeis-Sternwarte Bamberg
Friedrich-Alexander-Universität Erlangen-Nürnberg



Betreuer: Prof. Dr. Ulrich Heber und M.Sc. Matti Dorsch

Abstract

Hot subdwarf stars represent a late stage in the evolution of low-mass stars, which can not be described by canonical evolution of single stars and, therefore, they are likely formed by binary interactions. In this thesis I perform a radial velocity (RV) study of a sample of 2048 stars, consisting primarily of hot subdwarfs, but include a significant fraction of blue horizontal branch stars and white dwarfs of extremely low mass, based on spectra from the Sloan Digital Sky Survey (SDSS). Spectra, for each star, recorded at different times were available, but only for about half of the sample, the spectra were usable for the study of RV variability, due to their low signal to noise ratio. The detection probability is highly dependent on the observational time of the star. Only an insignificant fraction of 0.7% of variable stars were detected for observational times less than 2.5 h, while $\sim 10\%$ of all stars were detected to be in a binary for observational timespans longer than a day. I determined atmospheric parameters and radial velocities, by fitting grids of synthetic spectra, based on model atmospheres. This sample allowed me to study RV-variability as a function of the stellar parameters, effective temperature, surface gravity and helium content. The different stars were assigned to their different spectral classes, while most stars were subdwarfs of type sdB and sdOB. A striking finding is the completely different behaviour of helium poor and helium rich subdwarfs. While for the latter only one binary was detected, 52 binaries for helium poor stars were found. This leads to the conclusion, that there might be no evolutionary link between helium rich and helium poor subdwarfs. Intermediate helium and helium rich stars are more likely to be related as sdBs have almost the same fraction of detections. Subdwarfs of type B seem to evolve more likely in binaries than sdOs and sdOBs as they have the most significant fraction of detected RV variability. Blue horizontal branch stars do not show a significant fraction of RV variability, as only 4 were found in a binary. On the other hand extremely low mass white dwarfs have a similarly large fraction of radial velocity variables as sdB stars, which might be due to a similar evolutionary scenario.

Contents

1	Introduction	4
2	Stellar Evolution	6
2.1	Hertzsprung-Russell-diagram	6
2.2	Kiel diagram	8
3	Hot Subdwarfs	9
3.1	Characteristics	9
3.2	Evolution of hot subdwarfs	10
4	Sloan Digital Sky Survey	12
4.1	Mission	12
4.2	Telescope	13
4.3	Camera	14
4.4	Spectrographs	14
5	Methodology	18
5.1	Radial velocity and Doppler shift	18
5.2	Radial velocity variability	19
6	Data analysis	21
6.1	Fitting method and grids of synthetic spectra	22
6.2	Log p-value	23
7	Results	25
7.1	Example Fit for Variable stars	25
7.2	Radial velocity variable stars	26
7.3	Kiel-diagram	29
7.4	SDSS J183317.73+642737.1	31
7.5	Radial velocity variability depending on helium abundance	34
7.6	Radial velocity variability fractions by spectral type	36
7.7	Time distribution of observed data	37
7.8	Comparison with Mattig	38
8	Summary and outlook	41
9	Appendix	48

1 Introduction

Generally, stellar evolution seems to be quite well understood, like the evolution of our sun, which will become a red giant and end up as a white dwarf. However, this is in part not true, because some concepts of stellar evolution are only hardly understood, like binary evolution which is not uncommon. Especially in late stages of stellar evolution, for example for white dwarfs that reside in a binary, the physical occurrence is not clear. Among those objects, hot subdwarfs stand out, as they mostly evolve in binaries and as they are faint blue stars at high galactic latitudes. They have small masses of around $0.5M_{\odot}$ and their radii range from $0.1R_{\odot}$ - $0.3R_{\odot}$. Even if they are smaller and lighter than most main sequence stars, they are much hotter than main sequence stars, like our sun, which makes them very interesting objects for investigation and understanding of the complex evolutionary processes, as well as binary evolution. Hot subdwarfs often show radial velocity variability, because they often evolve in binary systems. However, the evolution of hot subdwarfs is not finally cleared. In general, there are two spectral types of hot subdwarfs. Type O and type B subdwarfs, which differ in temperature and characteristics in their spectra. Furthermore their evolution seems to be dependent on their helium abundance as well as their spectral class. Therefore, atmospheric parameters, like helium abundance and effective temperature as well as surface gravity were determined, which allowed to study the radial velocity variability as a function in the $T_{\text{eff}}\text{-log } g$ and $T_{\text{eff}}\text{-log}(\frac{n(\text{He})}{n(\text{H})})$ diagram on the basis of Geier et al. (2022). This serves to a better understanding of the complex evolutionary scenarios of stars, especially for the different types of hot subdwarfs.

For the analysis, the spectra of the stars in the sample, used in this thesis, which contained 2048 individual stars, were investigated for different abnormalities. For example, to derive the radial velocity the absorption lines of the spectrum are investigated on shifts, caused by the Doppler shift. The spectra are provided by the Sloan Digital Sky Survey (SDSS), which is carried out by a 2.5 m telescope in the US and has doubled the number of known hot subdwarfs. The blue and red spectra of the SDSS are fitted separately.

First of all, some theoretical background is discussed in section 2, like the stellar evolution and position of different stars in the Hertzsprung-Russell-diagram. In section 3, the focus is on the hot subdwarfs, where at first, the characteristics of different types of subdwarfs and then, the evolution of those stars are explained. The Sloan Digital Sky Survey is executed in section 4, while the methodology of how the spectra of the SDSS can be analyzed on the different parameters is explained in section 5. The data analysis, like the fitting method and the determination of the false detection probability, is shown in section 6. Finally, in section 7 the results

of the thesis are collected and the stars which show radial velocity variability are listed, as well as a comparison with Mattig (2022), who analyzed the same sample of stars like this thesis, but with a different fitting method. Furthermore the most interesting object SDSS J183317.73+642737.1 is discussed in this section and all stars are applied in a Kiel diagram. The dependency of helium abundances and variability, as well as the dependency between the spectral class and radial velocity variability of this sample is given in this section. The results are summarized and an outlook is given in section 8.

2 Stellar Evolution

In general, the lifetime of a star is much longer than the lifetime of a human being and even than the whole evolution of mankind. Sun-like stars, for example, have a lifetime of about ten billion years. This causes the fact, that human beings are only able to observe a small snapshot in the whole life of a star. Stars, undergo different lifestages, as well as human beings. Stars are born from a collapsing cloud of gas and dust. During their lifetime, a star produces energy by nuclear fusion, like the fusion of hydrogen atoms in the core, which produces helium. When the star is not able to perform nuclear fusion anymore, the star dies and ends up as a neutron star or a white dwarf. The evolution of those stars depends on the mass of the star and will be described in the next section.

2.1 Hertzsprung-Russell-diagram

To describe the population of stars, a Hertzsprung-Russell diagram (HRD) is helpful. This diagram was invented by Ejnar Hertzsprung in 1913 and was built upon works of Henry Russell. Normally, the HRD shows the absolute magnitude in dependence of the spectral class. Because of the relation between the absolute magnitude and the luminosity, and between the effective temperature of the star and its spectral class discovered later on, it is often shown as a plot of the luminosity over the effective temperature of the star as also shown in Figure 2.1. In the HRD the different lifestages of a star can be seen. But the path of a star in the HRD depends on its mass. When a star is born, it begins its evolution at the main sequence, which is shown as a diagonal in Figure 2.1. At this stage, a star produces energy by nuclear fusion burning hydrogen to helium. When all hydrogen is consumed, the star can't burn any hydrogen in the core anymore and just burns hydrogen in its shell now. This leads to the stars shell being expanded strongly and the star moves from the main sequence to the red giant branch in the HRD, as it becomes a red giant. At this point the star remains hydrogen burning in the shell until it reaches the tip of the red giant branch. For stars with masses of $< 2M_{\odot}$, helium fusion ignites in the core in a helium flash. This causes the star to contract and so it moves in the HRD to the horizontal branch by shrinking in radius and increasing its surface temperature. The star remains at this position in the HRD as long as all helium is burnt in the core. However, helium and hydrogen fusion continues at the shell, which causes the star to expand again and moving to the asymptotic giant branch. Afterwards, the star pushes off its shell in a planetary nebular, which causes very high temperatures at the surface of the star. The luminosity stays constant until the He-shell and then the H-shell dries up. Then the core is stabilised by the degeneration pressure of the electron gas and cools down. A white dwarf (WD) remains.

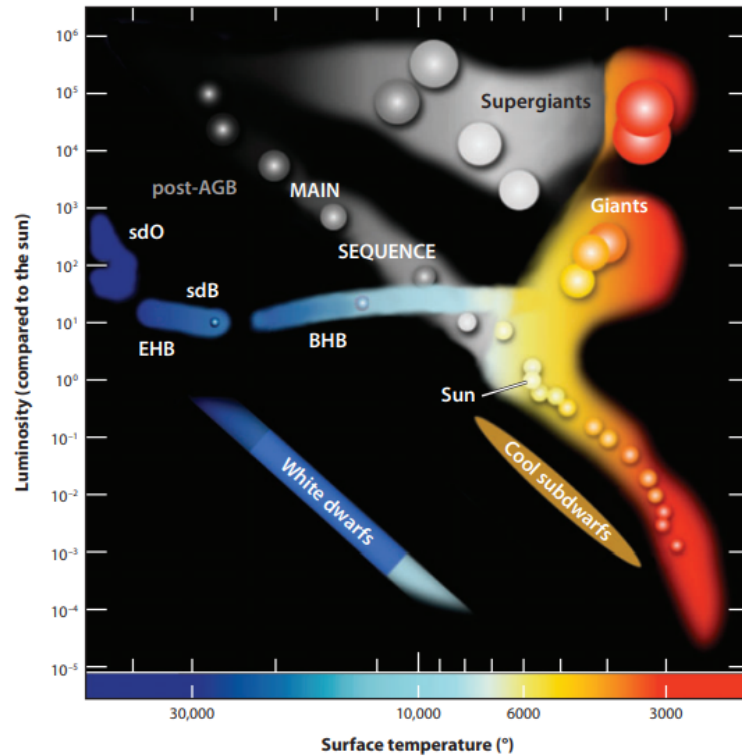


Figure 2.1: Sketch of a Hertzsprung-Russell-diagram, with luminosity plotted over the surface temperature. In this HRD the different kinds of populations are marked, where the main sequence is nearly diagonal. The giants and supergiants are settled for higher luminosities than the main sequence. The horizontal branch crosses the main sequence and becomes the blue horizontal branch stars (BHB) for higher temperatures. For even higher temperatures, the BHB becomes the extreme horizontal branch (EHB), where the subdwarfs of type O and B are located. White dwarfs are located parallel to the main sequence with higher temperatures and much lower luminosities. Cool subdwarfs are located nearly to the red and yellow stars at the main sequence (Heber; 2009).

The white dwarf mass distribution comprises a population of low-mass remnants. These stars are thought to be created by strong mass-loss episodes in interactive binary systems before the helium flash during the red giant branch-phase of low-mass stars. However, the origin of those stars remains a puzzle (Heber; 2017). Specifically, an interactive binary evolutionary scenario is thought to be the most plausible origin for the so-called extremely low-mass (ELM) white dwarfs, which have masses below $\sim 0.18 - 0.30M_{\odot}$ (Calcaferro et al.; 2018). The progenitors of

those ELMs, are the so called pre-ELM WDs, which are less common than the ELMs, as they evolve faster.

For stars with masses of more than $8M_{\odot}$ the evolutionary process is quite different and they end in an supernova and the collapsed cores become a neutron star or a black hole.

2.2 Kiel diagram

As in the HRD, different stages of stellar evolution can be studied in a Kiel-diagram. The difference to the HRD is that the luminosity on the y-axis is exchanged with the surface gravity $\log g$, which means that the Kiel diagram only shows directly measurable parameters (see subsection 7.3). In a sample of hot subdwarf stars, pre-ELMs can sometimes appear, as they are settled in almost the same region in the Kiel diagram, like hot subdwarfs. In Figure 2.2 the position in the Kiel diagram of the pre-ELM HD 188112 can be seen next to the subdwarf stars. HD 188112 is a little cooler than the hot subdwarfs but is in the same range for $\log g$ at around 5.7.

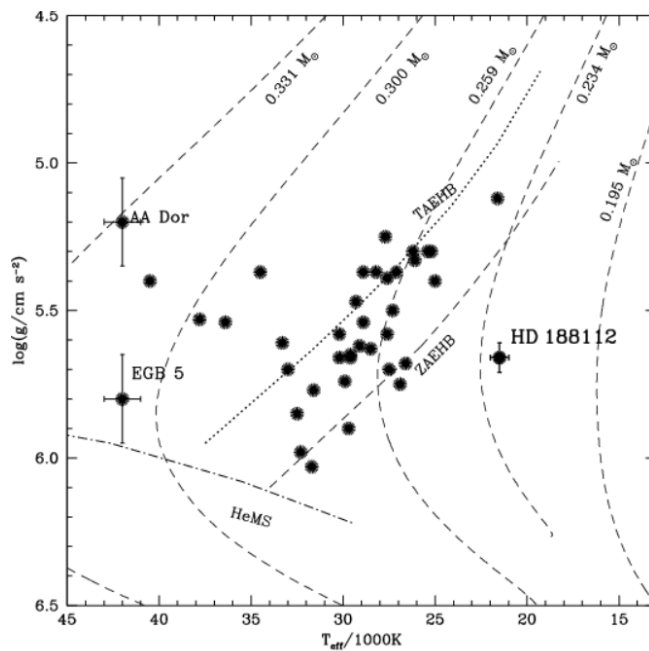


Figure 2.2: Position of the pre-ELM WD HD 188112 next to the hot subdwarfs in the Kiel diagram (Heber et al.; 2003).

3 Hot Subdwarfs

Hot subdwarfs are not formed by the classical evolutionary channels, described in the previous section. They are core helium-burning stars at the blue end of the horizontal branch (see Figure 2.1) or have evolved even beyond that stage (Heber; 2016). This thesis will focus on those stars.

3.1 Characteristics

In general hot subdwarfs have masses of around $0.5 M_{\odot}$ and their radii are in range of $0.1 - 0.3 R_{\odot}$ (Geier et al.; 2022). They reach temperatures of $20000 - 70000 K$. Therefore hot subdwarfs can be split into two parts:

- **sdB-stars:** Cooler subdwarfs with surface temperatures between 20000-40000 K. The spectra of sdB stars are normally very homogeneous and show the Balmer-lines, but show, in contrast to main sequence stars, just weak helium I lines and no helium II lines.
- **sdO-stars:** Hotter subdwarfs with surface temperatures of more than 40000 K. They display the He II line at 4686 \AA , and sometimes other He II lines in addition in their spectra. It is also possible that the Balmer lines are absent in some cases, especially for extremely helium rich sdOs.

Subdwarfs of type O and B have little in common with the main sequence O and B stars. With their small radii, they do not have as high luminosities as main sequence O and B stars. Furthermore the masses of hot subdwarfs are much smaller than for main sequence O and B stars.

B type subdwarfs are located on the extreme horizontal branch and about 33% are found in close binaries (Napiwotzki et al.; 2004), (Copperwheat et al.; 2011). Their atmosphere show low helium abundances and hence they are normally helium poor. Subdwarfs type B seem to be more common than sdO stars and outnumber those sdOs by a factor of 3, as Green et al. (1986) found out.

Subdwarfs of type O differ from the normally helium-poor sdBs as their atmospheres are often enriched with helium.

SdOB stars are another kind of subdwarfs, which have sdB like spectra but show a weak He II line at 4686 \AA . Type OB subdwarfs normally have higher helium abundances than most sdBs, but still below solar. There are also He-sdBs, but they are rare (Heber; 2009)

In this thesis, the subdwarfs are divided into three classes according to their helium abundances. One type are helium poor subdwarfs, where the helium abundance

is smaller than solar helium ($< \frac{He}{H} = \frac{1}{10}$). The other ones are helium rich subdwarfs. Those are divided in intermediate helium subdwarfs (iHe), which have helium abundances between solar helium and $\frac{He}{H} = 4$ and helium rich subdwarfs with an even higher helium abundance.

3.2 Evolution of hot subdwarfs

As a significant part of sdBs reside in binaries, it is, therefore, clear that binary evolution plays an important role in the hot subdwarf evolution. But in contrast to the sdB stars, sdO stars do almost never reside in binary systems (Napiwotzki; 2008). This is an indicator, that different evolutionary channels are possible in the evolution of hot subdwarfs. The three evolutionary channels of hot subdwarfs are:

- **Stable Roche-lobe overflow:** If the masses of the two stars in a binary system are similar ($\frac{M_2}{M_1} < 1.2 - 1.5$) a stable-Roche overflow can happen. Starting from the main sequence, a star becomes a red giant and gets bigger than its Roche lobe, which is the region around the star in a binary system, where the orbiting material is gravitational bound to the red giant. Therefore the red giant transfers parts of its mass to the other star. This process can be the origin of sdB stars in wide binaries with a period of 10-500 days (Geier; 2015). The orbital period depends on how angular momentum is lost from systems with the shortest periods (Han et al.; 2003). This process is shown in Figure 3.1 at point (C).
- **Common envelope scenario:** The common envelope scenario happens after an unstable mass transfer from the red giant to its neighbor. This happens when the masses of the stars are not similar at the beginning ($\frac{M_2}{M_1} > 1.2 - 1.5$). Those binaries normally have a very short period of 0.1-10 days (Geier; 2015). This scenario can be seen in Figure 3.1 at points (A) and (B). It can also happen when the masses of the two stars are similar ($\frac{M_2}{M_1} < 1.2 - 1.5$). Then the heavier star becomes a red giant and transfers its mass to the lighter one. The red giant becomes a white dwarf afterwards, but the lighter star becomes much heavier, caused by the transferred mass. Now this star becomes a red giant too and an unstable mass transfer occurs. Hence, both stars share their outer layers of gas, while the cores orbit inside the shared shell forming a common envelope around the binary system. After some time, the shell gains enough energy and angular momentum by friction to be ejected from the system and a binary system with a sdB and a white dwarf remains (Heber; 2016).
- **White dwarf mergers:** The creation of a single sdB or sdO is also possible by white dwarf mergers. This evolutionary channel is based on two helium

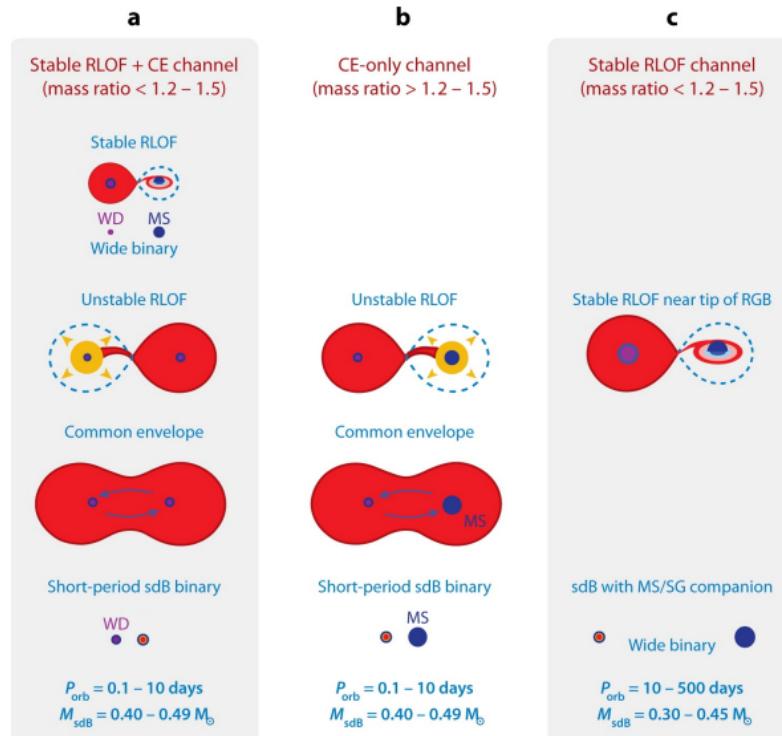


Figure 3.1: Different evolution channels for sdB stars. Point C describes the stable-Roche overflow. Point B shows the common envelope scenario. Point A is a mix of both of them (Heber; 2016).

white dwarfs in a binary, which might be evolved by two common envelope phases or one stable Roche-lobe overflow phase and one common envelope phase, according to Han et al. (2003). When those white dwarfs are in a very close orbit, gravitational radiation (gravitational waves) will be emitted. Due to this, the binary system loses angular momentum and the system shrinks. So the two helium white dwarfs may coalesce, when a mass transfer from the primary to the secondary white dwarf happens. When the merger product ignites helium (shell flash), the radius and the luminosity increases, so that the star becomes a yellow giant. When the yellow giant reaches a specific mass, the helium shell moves inwards and the effective temperature increases, which leads to the formation of a single subdwarf star. (Zhang and Jeery; 2012; Han et al.; 2003; Saio and Jeery; 2000).

4 Sloan Digital Sky Survey

The Sloan Digital Sky Survey (SDSS) provides the spectra of the sample of stars studied in this thesis. Program stars are selected from the 56th version of the subdwarf catalogue by Geier (2020). The SDSS is carried out with a 2.5 m telescope at the Apache Point Observatory in New Mexico in the US. The planning for the SDSS began in the mid 1980s and was finally started in 2000 (Gunn et al.; 2006). It was named after Alfred P. Sloan, who created a foundation to support the survey. The SDSS consists of a multi filter scanning CCD camera to image the sky at high efficiency and of two multi fiber spectrographs, which are able to take spectra of 640 objects at the same time for the SDSS spectrograph. The SDSS spectrograph was exchanged by the BOSS spectrograph, which is able to take spectra of 1000 stars at the same time (Kent; 1994).

4.1 Mission

The mission of the SDSS consists out of different phases. The first phase began in 2000 and lasted until 2005. During the first phase, SDSS imaged around 8000 square degrees in the sky and took spectra of galaxies and quasars, which were pre-selected by the imaging.

In the second phase, from 2005-2008 the survey was extended to explore the structure of the Milky Way. Therefore, the survey was divided into three parts. The SDSS Legacy survey provided a uniform map of more than 7500 square degrees of the North Galactic Cap and three stripes in the South Galactic Cap. Almost all of this data were obtained in the first phase but a small part of the footprint was finished in the second phase (<http://classic.sdss.org/legacy/index.html>; 2014). The Sloan Extension for Galactic Understanding and Exploration created a three dimensional map of the Milky Way by obtaining spectra of 24000 stars (<http://segue.uchicago.edu/>; 2007). The third part was the Sloan Supernova Survey. It performed repeated imaging in the southern galactic cap to search for Type Ia supernovae, which are supernovae that occur in binary systems, where one of both stars is a white dwarf. It found more than 500 type Ia supernova (Sako et al.; 2007).

The third phase SDSS-III, contained four parts and took part from 2008-2014:

- 1.) The APO Galactic Evolution Experiment used infrared spectroscopy to penetrate the dust of the disk and bulge of the Milky Way (<http://www.sdss3.org/surveys/apogee.php>; 2013).
- 2.) The goal of the Baryon Oscillation Spectroscopic Survey was to measure the expansion of the universe.

3.) The Multi-object APO Radial Velocity Exoplanet Large-area Survey determined the radial velocity of 11000 bright stars to generate a statistically well-defined sample of massive planets with thick hydrogen and helium atmospheres (<http://www.sdss3.org/surveys/marvels.php>; 2013).

4.) The Sloan Extension for Galactic Understanding and Exploration 2 built up on the first part and observed around 120000 stars from distances between 10-60 kpc (<http://www.sdss3.org/surveys/>; 2013).

The fourth phase (SDSS-IV) from 2014-2020 contains the eBOSS, which describes a cosmological survey of quasars and galaxies and also surveyed variable objects. It also provides some of the spectra, which were used in this thesis.

4.2 Telescope

For imaging and spectroscopy, the SDSS uses a dedicated 2.5 meter f/5 telescope (see Figure 4.1) (York et al.; 2000).

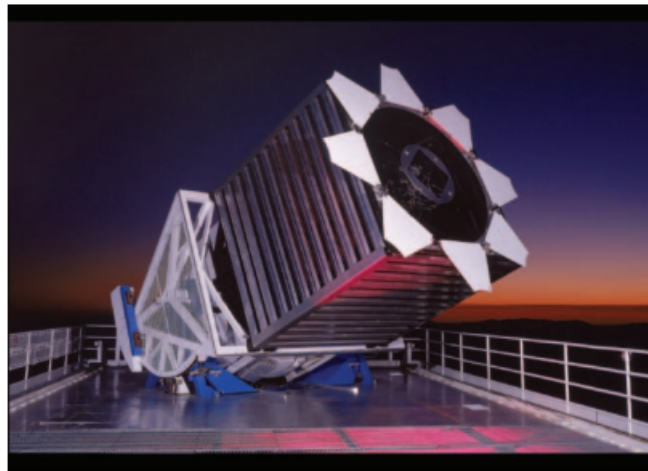


Figure 4.1: SDSS 2.5 meter telescope at sunset (Gunn et al.; 2006).

The telescope achieves a 3° distortion free field of view with a large secondary mirror and two corrector lenses. The principle of this telescope is shown in Figure 4.2 and is taken from (<http://www.sdss.org/background/telescope.html>; 2006).

It is equipped with a photometric/astrometric mosaic camera (Gunn et al.; 1998) and two double fiber-fed spectrographs. Besides the 2.5 m telescope, it has three subsidiary instruments at the side. One is the photometric telescope, to calibrate the photometry. Furthermore it has a seeing monitor and a cloud scanner, which monitor the astronomical weather.

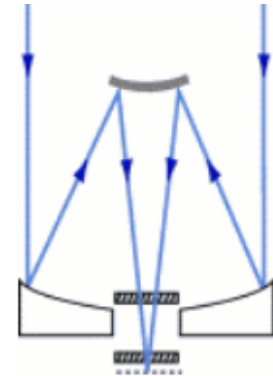


Figure 4.2: Image that shows how the light is guided through the telescope.

4.3 Camera

The SDSS imaging camera contains two sets of CCD arrays, the imaging array and the astrometric arrays (York et al.; 2000). The imaging array is the main part of the camera and provides the photometric brightness of a star. It contains thirty 2048×2048 CCDs, which are placed in six columns with 5 rows. The scanning of the telescope is aligned with the columns. They are two inches square. In total this number corresponds to around 120 megapixels according to <http://www.sdss.org/background/telescope.html> (2006).

Each row is equipped with a different filter, named u' , g' , r' , i' and z' , also shown in Figure 4.3. So, each row observes the sky with a different wavelength. These central wavelengths for the u' , g' , r' , i' and z' filters are 3560, 4680, 6180, 7500 and 8870 Å (Fukugita et al.; 1996). Those filters are placed in the camera at the order of r', i', u', z', g' . Furthermore the camera is cooled down to -80°C to reduce the noise. The imaging survey is taken in drift scan, which means that the camera sweeps the sky in great circles all the time.

4.4 Spectrographs

The photometric data were used to select objects, like stars and galaxies for the spectroscopy. Each SDSS spectrograph utilizes a dual-channel design with a common reflecting collimator and a dichroic to split the beam into a blue and red channel. In each channel, just downstream of the dichroic, a transmitting grism disperses the light, which is imaged by an all-refractive camera onto a CCD. The two spectrographs of the SDSS are mounted to the telescope. Fiber-fed multi-object spectrographs were used to acquire a large number of spectra simultaneously over a large field of view (Smee et al.; 2013). For the SDSS spectro-

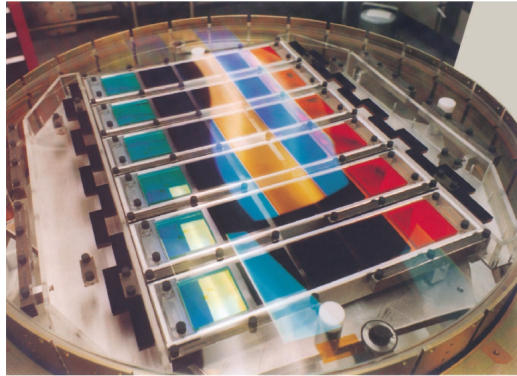


Figure 4.3: Camera of the SDSS, with the different filters in the order of 5 rows and 6 columns (Gunn et al.; 1998)

graph, 640 holes were drilled into an aluminium plate, where each hole corresponds to the position of a selected object, according to (Newman et al.; 2004).

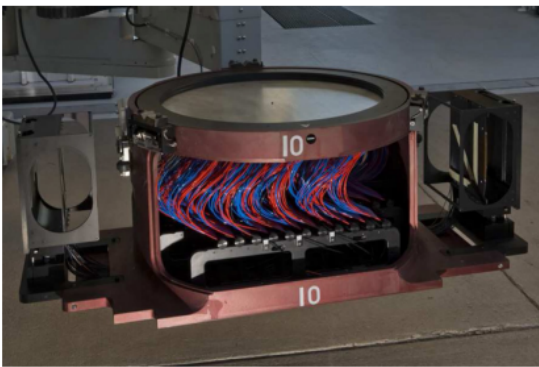


Figure 4.4: Fibers mounted to the aluminium plate, which are routed in bundles to the slitheads of the spectrographs (apparatuses on the right and left side of the fibers) (Smee et al.; 2013)

The optical fiber cables were plugged into those holes, to capture the light from the 640 objects and send it to the two slitheads of the two spectrographs simultaneously. The fiber cables mounted in the aluminium plate can be seen in Figure 4.4. The two spectrographs are built identically and split the light. The resulting spectra are recorded by CCDs, which measure the wavelengths in a range of 3800 Å to 9200 Å. A dichroic beamsplitter divides the incident collimated beam, reflecting the blue portion of the band-pass ($\lambda < 6000\text{Å}$) and transmitting the red wavelengths ($\lambda > 6000\text{Å}$) to increase the resolution of the spectro-

graph (Smee et al.; 2013). The throughput for the different wavelengths is shown in Figure 4.5.

The blue and red spectrum is recorded by a separate CCD, which has 2048x2048 pixels (*The SDSS Instruments*; 2005). To clarify, how this thesis, Figure 4.6 might be useful. The fiber cables, which send the light from the objects to the spectrograph, are connected to the slithead of the spectrographs. From this point on, the light propagates to the collimator, where the light is mirrored in nearly parallel

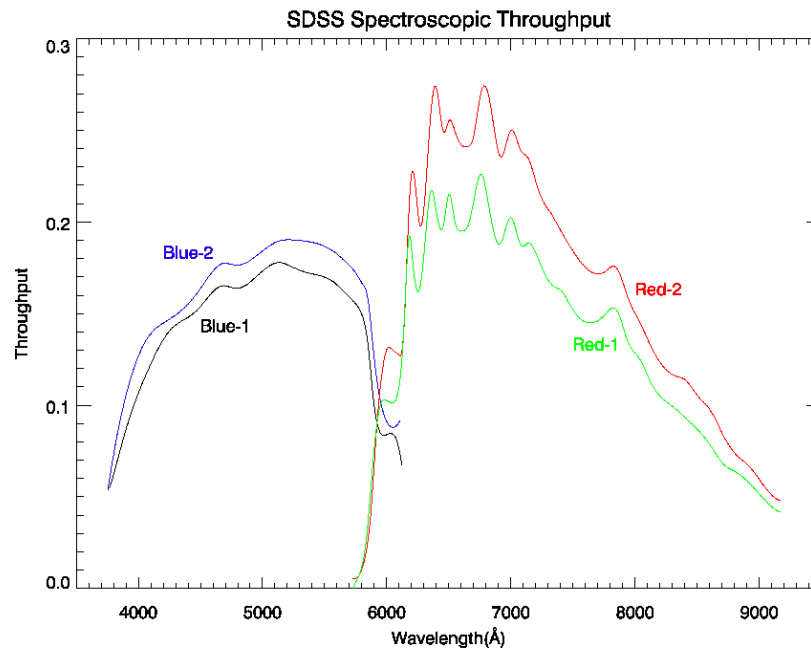
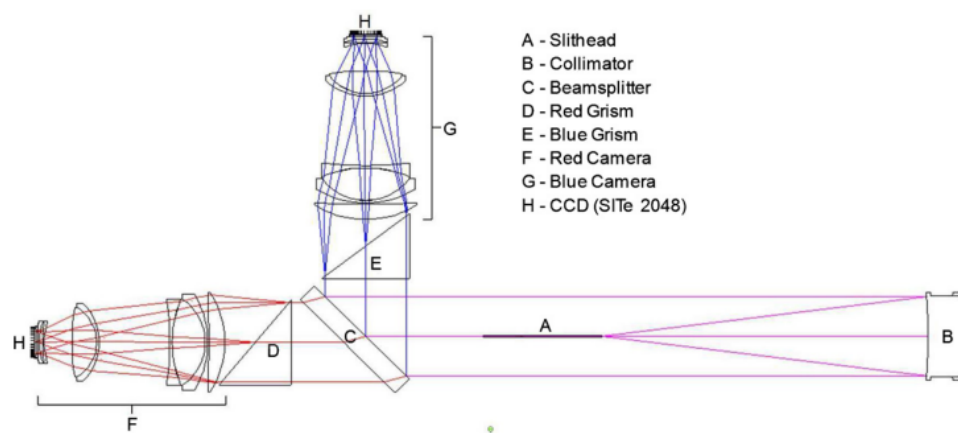


Figure 4.5: Throughput of the different wavelengths of the SDSS spectrograph (<https://classic.sdss.org/dr7/instruments/spectrographs/index.html>; 2003).

rays until it reaches the beamsplitter, with a special coating. The beamsplitter reflects the blue part of the light, while it lets transmit the red part. The two parts of the incoming light have to pass a grism, which is a combination of a grid and prism. It splits the blue and red part of the light in its different wavelengths. The light is focused in the camera on the CCD, where the spectrum is created (in total 4 spectra, one blue and one red one for each spectrograph). It is possible to obtain spectra for up to 5000 objects in one night with this spectrograph (Smee et al.; 2013).

For the BOSS spectrograph, the basic optical design has been retained, with several improvements. The ruled gratings have been replaced by volume-phase holographic (VPH) gratings (gratings sandwiched between two prisms) and the CCDs have been replaced by more modern devices. These changes produce a significant improvement in throughput and a modest extension of the wavelength range in both, the blue and red channels (Smee et al.; 2013).



- A - Slithead
- B - Collimator
- C - Beamsplitter
- D - Red Grism
- E - Blue Grism
- F - Red Camera
- G - Blue Camera
- H - CCD (SiTe 2048)

Figure 4.6: Schematic depiction of the spectrographs. The light from the fiber cables gets inside the slitheads(A). It propagates to the Collimator (B), which mirrors the light to the beamsplitter (C), where the light is split into a red and blue part. After that the two parts of light pass the gratings (D,E), where they are split again in different wavelengths and focused on the lenses of the camera (F,G) until it reaches the CCD (H)(Smee et al.; 2013).

5 Methodology

This thesis is built up on the work of Geier et al. (2022), which analyzed a sample of 646 hot subdwarfs on radial velocity variability, while the atmospheric parameters were taken from literature. The spectra of Geier et al. (2022) were taken from the SDSS and from the Large Sky Area Multi-Object Fibre Spectroscopic Telescope (LAMOST), while in this thesis only the spectra from the SDSS were analyzed. Geier et al. (2022) determined the radial velocity by fitting separate lines with approximated lineprofiles. In contrast to Geier et al. (2022), atmospheric parameters ($\log g$, surface temperature T_{eff} and the helium abundance) were determined with the fitting method used in this thesis, that fitted the global spectrum by using synthetic spectra and grids (see subsection 6.1). As in Geier et al. (2022) the false detection probability $\log p$ was used to determine the variability of a star. The different helium abundances were divided into helium rich, intermediate helium and helium poor stars, as also done in Geier et al. (2022).

The most important tool for the study of variable stars is to determine the radial velocity. A basic to derive the radial velocity with the spectra is the Doppler shift, which is explained in the next section

5.1 Radial velocity and Doppler shift

The velocity \vec{v} of stars relative to us, can not be measured directly. Its absolute value is composed of two components, the radial velocity \vec{v}_{rad} and the tangential velocity \vec{v}_{tan} :

$$|\vec{v}| = v = \sqrt{v_{\text{tan}}^2 + v_{\text{rad}}^2} \quad (1)$$

The distribution of the velocities are shown in Figure 5.1. When the radial velocity is $v_{\text{rad}} > 0$, the star moves away from us and for negative radial velocities it moves towards us. The radial velocity can be determined directly by measuring the Doppler shift of the spectral lines. If the star moves towards us the spectral lines have shorter wavelengths than normal (blueshifted) and when it moves away from us the wavelengths become larger (redshifted). Normally the Doppler shift is given for frequencies, but with the equation

$$\lambda = \frac{c}{f} \quad (2)$$

where λ is the wavelength, c the speed of light and f the frequency. With that, the radial velocity can be calculated with

$$v_{\text{rad}} = c \cdot \frac{\Delta\lambda}{\lambda} \quad (3)$$

where $\Delta\lambda$ is the wavelength difference to the true wavelength λ .

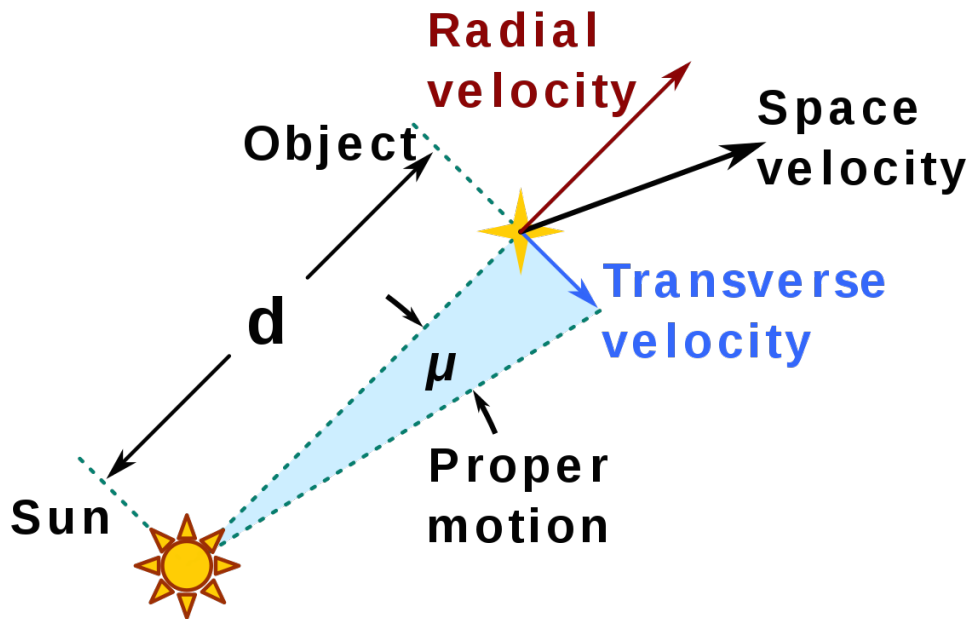


Figure 5.1: Distribution of the absolute (space velocity), tangential and radial velocities (<https://commons.wikimedia.org/wiki/File:Propermotion.svg>; 2018).

5.2 Radial velocity variability

The determination of the radial velocity helps to detect binaries. Two stars orbit around their centre of mass in a binary. A binary can be detected, when the radial velocity is displayed over time and it varies, caused by the Doppler shift. This effect is called radial velocity variability. Therefore two different kinds of binaries have to be distinguished from each other. Single lined binaries (Type: SB1), are binaries where only one component can be recognized in the spectrum. In type SB2 binaries, also called double lined binaries, both stars can be seen in the spectrum. For binary systems some measurements at different times are needed. A radial velocity curve can be created, by which the period can be derived if the system

is observed for long enough. SB1 binaries are the most common type of binaries. In contrast to SB1 systems, the radial velocities of both stars can be measured in SB2 systems. Therefore, the variation of absorption lines of one star have to be measured separately from the absorption lines of the other star (Popova et al.; 1982). However, no SB2 system was found in the sample of stars under study. To clarify how the Doppler shift can be seen and different radial velocities can be determined with the absorption lines of the spectra, an exemplary comparison of the H_γ lines, for different times, is shown in Figure 5.2. In this case, it is possible to see the shift of the lines for different times with naked eyes. But it also shows how sensitive the fitting method has to be, to detect those small differences of the shift to be able to calculate the radial velocity. The example contains spectral fits for the star "SDSS J075610.71+670424.6", which was contained in the sample of this thesis. Therefore the H_γ -line without any Doppler shift is shown as black line, to clarify how the lines are shifted by the Doppler shift.

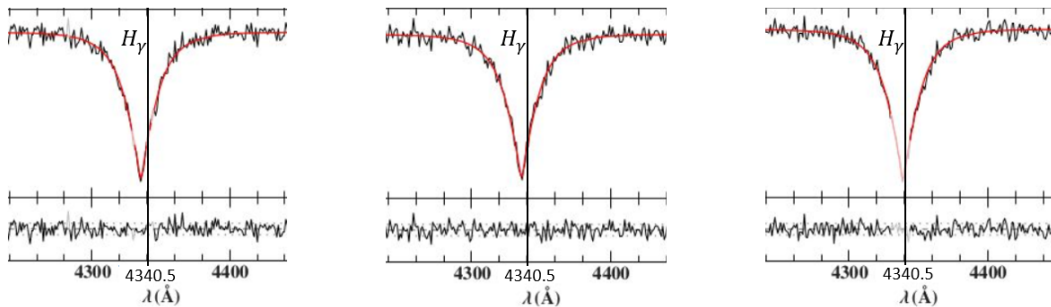


Figure 5.2: Spectral fit to a part of the spectra of the detected variable star SDSS J075610.71+670424.6 obtained at different times for the H_γ line. The laboratory wavelength of the H_γ line is shown as a vertical black line. The plot shows the comparison of the absorption lines, which are shifted by different radial velocities.

For SB1 and SB2 binaries the detection probability is strongly dependent on their period, as most surveys do not observe stars for a long time. So the probability to detect a binary is very low for spectra recorded in few intervals much shorter than their orbital period and higher for spectra recorded with multi epoch observations. To visualise the period distribution of known variable hot subdwarfs, Kupfer et al. (2015) created a histogram. Figure 5.3 shows the number of known subdwarf binaries as a function of their orbital period. Known binaries have a period of 0.05 to 30 days, with a maximum at around 1 day.

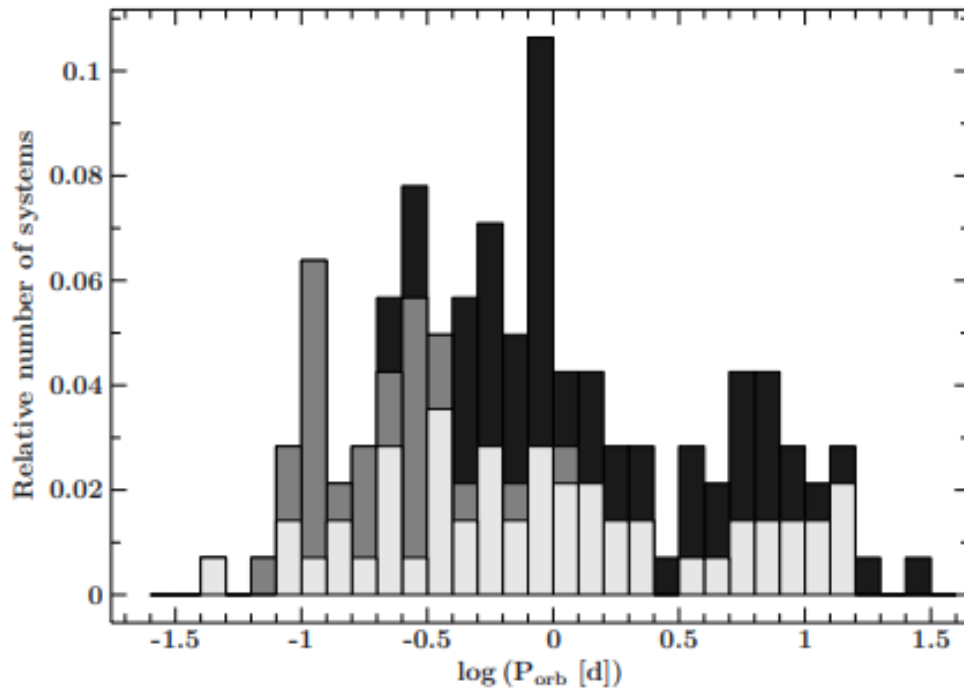


Figure 5.3: Distribution of the periods of detected variable systems. The period is shown as $\log(\text{period})$ in days. The different colors of the bars stand for different types of companions (light grey: white dwarf companion, grey: low mass main sequence companion and dark grey: unknown companion type)(Kupfer et al.; 2015).

6 Data analysis

The public archive of SDSS provides the user with spectra co-added from all individual observations and combined spectroscopic channels. In order to search for radial velocity variations, however, individual spectra were needed. Dr. Ingrid Pelisoli provided single spectra, the red and the blue part of the spectra. Those spectra were analyzed and fitted. However, later on, the red part of the spectra were sorted out for analyses, because the signal noise ratio of the red part was very low and RVs turned out to be spurious. Therefore only the blue part was used for the search of variable stars. Furthermore, blue spectra with a signal noise ratio < 5 are not usable and were sorted out, too.

6.1 Fitting method and grids of synthetic spectra

The fitting method was developed by Irrgang et al. (2014) and makes it possible to determine atmospheric parameters and the radial velocity at the same time.

Since the fitting method in this thesis is based on model atmospheres, calculated with the hybrid LTE/NLTE method described by Irrgang et al. (2018), grids of synthetic spectra were fitted to the spectra. One used grid is for the sdB stars, for effective temperatures of 15000-55000 K, $\log g$ of 4.6-6.6 and $\log n(\text{He})$ of -5.05 to -0.041. A grid for the ELMs with temperatures ranging from 9000 to 20000 K, $\log g$ from 3 to 7 and $\log n(\text{He})$ ranging like the sdB grid. The third grid was for the hot sdO stars and its range for temperatures is 51000-75000 K, for $\log g$ 5.2-6.6 and for $\log n(\text{He})$ like in the other grids. Those grids were calculated by U. Heber.

The used fitting method is a grid-based global fitting method that facilitates quick and precise determinations of the atmospheric parameters (T_{eff} , $\log g$ and $\log n(\text{He})$). It is based on fitting grids of synthetic spectra to observation by using the concept of χ^2 -minimization. Normally, investigations of atmospheric parameters are time consuming, because an iterative process is required. Elemental abundance for elements other than hydrogen and helium were fixed to the typical metal abundance distribution as given by Jery et al. (2013). The radial velocity is incorporated afterwards by shifting the entire wavelength scale according to the Doppler formula (see subsection 5.1)(Irrgang et al.; 2014). Some of the analyzed stars ended up at a border of a grid, especially at the $\log g$ upper limit of the sdB grid at 6.6. All stars, that ended up at this value were sorted out, because those are kind of stars, on which this thesis is not focused on. Other stars ended up at the upper limit of the helium abundance at -0.041. These are eHe-sdOs and so they are interesting for the study and need to be re-investigated with a different grid to determine their true atmospheric parameters(see subsection 7.3 and Table 9).

To compare those models with observations, the synthetic spectra are convolved with a Gaussian curve. The goodness of the fit of a model can be derived with the observed flux f_i , the model flux $f_{\text{model},i}$ and the uncertainty in the observed flux at data point i δ_i . The sum is taken over all pixels i in the spectrum.

$$\chi^2 = \sum_i \chi_i^2 = \sum_i \left(\frac{f_i - f_{\text{model},i}}{\delta_i} \right)^2 \quad (4)$$

The best possible value of χ^2 is 1. The nearer the value gets to 1, the better the quality of the fit. The χ^2 surrounding is generally very well behaved so that the absolute minimum is found after a relatively small number of steps, which allows

for quick and efficient analyses (Irrgang et al.; 2014).

It requires the knowledge of uncertainties of the measurement, either systematic or caused by statistical fluctuations such as noise n_i , to calculate χ^2 . The noise can be estimated from an observed spectrum, when assuming n_i obeys a Gaussian probability distribution $p(n_i)$ with a mean value of zero and an unknown standard deviation σ_i , which is the statistical component of the uncertainty δ_i in Equation 4 (Irrgang et al.; 2014):

$$p(n_i) = \frac{1}{\sqrt{2\pi}\sigma_i} \cdot \exp\left(-\frac{n_i^2}{\sigma_i^2}\right) \quad (5)$$

"For only several datapoints, the measured flux f_i as a function of the wavelength can be approximately written as a sum of $a + b\lambda_i$, which represents the first two terms in a Taylor expansion of the pure signal and a noise component n_i " (Irrgang et al.; 2014):

$$f_i = a + b\lambda_i + n_i \quad (6)$$

To estimate the noise level σ_i , the quantity Δ_i is defined as

$$\Delta_i = n_i - w_{i-2}n_{i-2} - w_{i+2}n_{i+2} \quad (7)$$

where $w_{i\pm 2}$, are weight factors, that are chosen so that all terms including λ are cut out and only the terms with noise remain. $p(\Delta_i)$ simplifies to

$$p(\Delta_i) = \frac{1}{\sqrt{2\pi}\bar{\sigma}} \exp\left(-\frac{\Delta_i^2}{2\bar{\sigma}^2}\right), \quad \bar{\sigma} = \sigma \sqrt{w_{i-2}^2 + w_{i+2}^2 + 1} \quad (8)$$

With that σ , which is the statistical component of δ_i of Equation 4 can be derived from the measurable distribution of Δ_i (Irrgang et al.; 2014).

6.2 Log p-value

Analogous to Geier et al. (2022), the false detection probability p is the most meaningful parameter for the detection of binaries in this thesis. The detection of RV variability is considered to be significant, if the false detection probability p is smaller than 0.01% ($\log p < -4$). When the false detection probability of a star is in range of 0.01% and 5% it is classified as a candidate for RV variability (Geier et al.; 2022). This value is well suited to describe the degree to which a star shows variations in its radial velocity as a singular variable (Maxted et al.; 2001). To calculate the false detection probability, the χ^2 -statistic has to be evaluated like described in Equation 4. In this case it is done for the velocities. Therefore the

mean of the radial velocities of a star has to be calculated and is defined as

$$\bar{v} = \frac{\sum_i \left(\frac{v_{\text{rad},i}}{v_{\text{err},i}} \right)}{\sum_i \left(\frac{1}{v_{\text{err},i}} \right)} \quad (9)$$

v_{rad} are the radial velocities and v_{err} are the corresponding uncertainties, which were calculated by the fit and a systematic error of $10 \frac{\text{km}}{\text{s}}$, was added. The corresponding χ^2 values can then be calculated from

$$\chi_i^2 = \left(\frac{v_{\text{rad}} - \bar{v}}{v_{\text{err}}} \right)^2 \quad (10)$$

Furthermore the number of degrees of freedom k has to be calculated, which is equivalent to the number of values that are free to vary independently. This results in

$$k = n_{\text{data}} - n_{\text{fit}} = n_{\text{data}} - 1 \quad (11)$$

n_{data} is the number of measured radial velocities and n_{fit} is the number of free parameters, which is one in this case, as \bar{v} is the only free parameter.

With all those parameters the false detection probability can now be determined with the cumulative distribution function (CDF) for the, with Equation 11 calculated, degrees of freedom k . χ^2 -CDF gives the probability to get a smaller $\sum_i \chi_i^2$ than the one passed to the function from radial velocities that are random fluctuations. The false detection probability is then

$$p = 1 - \text{CDF}_k \left(\sum_i \chi_i^2 \right) \quad (12)$$

and is equivalent to the probability of obtaining the same or higher summed values of χ^2 via random fluctuations. The code to calculate $\log p$ was provided by M. Dorsch.

7 Results

In this thesis, a hot subdwarf sample of 2048 stars was studied. This enabled information about the insights of the population and points out interesting objects, as well as detecting new binaries, to be obtained. The blue and red part of the spectra were fitted separately. However, the red spectra were sorted out afterwards, due to a low signal to noise ratio (see subsection 6.1). Stars were withdrawn from the sample, for which all spectra were too poor. 1231 stars with spectra remained using this condition. Those spectra were used for the determination of their radial velocity for all times, where the spectra were recorded, and their atmospheric parameters (T_{eff} , $\log g$ and the helium to hydrogen abundance ratio $\log(\frac{n(\text{He})}{n(\text{H})})$). In some cases the fit ended up at the upper limit of the surface gravity ($\log g=6.6$) (see subsection 6.1). Those stars were sorted out afterwards, too, because they can not be hot subdwarf stars, which this thesis wants to target. A total of 1095 stars remained. The results of the spectral analysis of those stars are discussed in the following sections.

7.1 Example Fit for Variable stars

To determine the radial velocity of a subdwarf over time, different spectra for different times were fitted. By using the Doppler formula, the radial velocity of each spectrum could be determined. An example of a spectral fit for the detected variable sdB SDSS J133040.91-001710.7 is shown in Figure 7.1, where the Balmer series can be seen very nicely, as well as the weak Helium I absorption line. The different absorption lines are also marked and named in the figure.

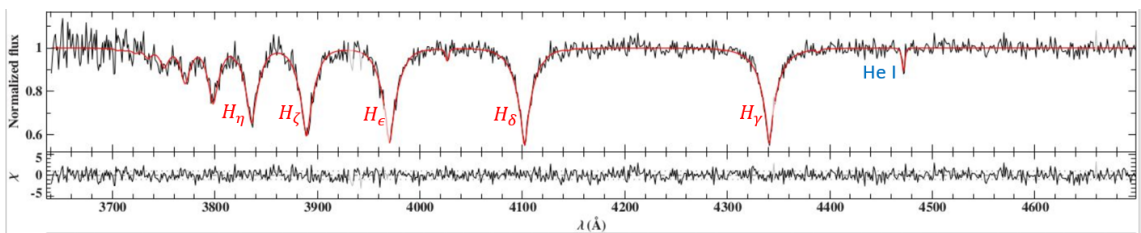


Figure 7.1: Spectral fit to the spectrum of the detected variable star SDSS J133040.91-001710.7. The different hydrogen absorption lines, as well as the He I absorption line are marked in the figure. The red line shows the best fit of the synthetic spectrum

The plot of the radial velocity over time (Figure 7.2) shows the RV variability of SDSS J133040.91-001710.7, which ranges from $-93 \frac{\text{km}}{\text{s}}$ to $87 \frac{\text{km}}{\text{s}}$. For this star, the Doppler shift of its absorption lines is presented in Figure 5.2

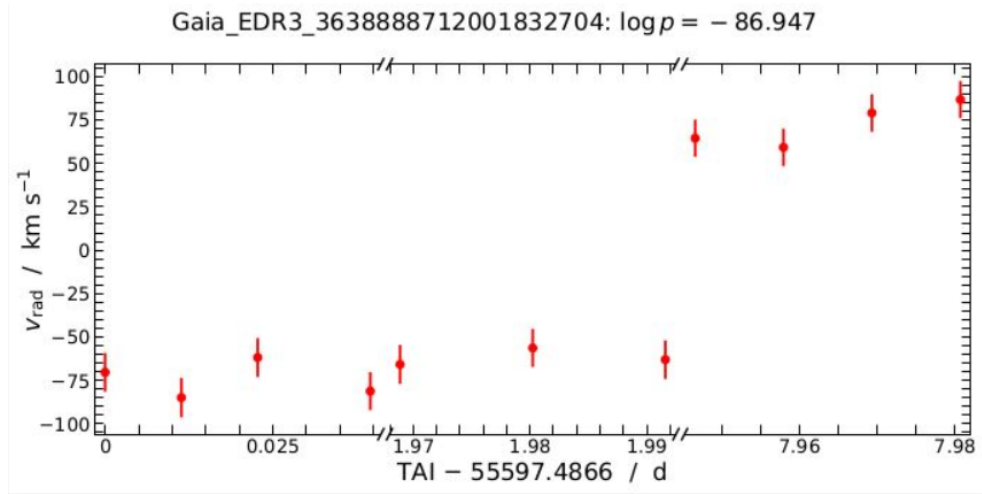


Figure 7.2: Radial velocity plotted over international atomic time for SDSS J133040.91-001710.7. Note the broken axis. The zero point of the time axis is the time of the earliest observation. Its Gaia designation is also given along with its $\log p$ value (-86.947). It can be seen that the star shows highly significant RV variations

7.2 Radial velocity variable stars

In total, 53 out of 1095 stars were detected to be radial velocity variable in this thesis ($\log p < -4$). Out of those, 37 were not known to be variable before. Those are listed in Table 1. The other 16 stars, which were known before to be variable are listed in Table 8 in the appendix. Further 44 objects are classified as candidates (where $-4 < \log p < -1.3$). The candidates are listed in Table 7. Atmospheric parameters (T_{eff} , $\log g$ and helium abundance) are given in all three tables, as well as the $\log p$ values. The names are shortened in the tables without their SDSS nomenclature (for example: SDSS J094750.71+162731.7 becomes to J094750.71+162731.7). As examples of detected variable stars, the RV curves over time are shown in Figure 7.3 for SDSS J140118.80-081722.6 and in Figure 7.4 for SDSS J064916.11+383419.7. The fact that some stars were detected as variables before, is a good check for the validity of the method used in this thesis.

The detected variable stars correspond to a fraction of 4.8 %, which is less than expected (Geier et al. (2022) found a fraction of 33% for sdB stars to be variable). This can be caused by several reasons. Only a fraction of the stars have spectral data for more than a epoch, so that no RV variability can be detected in this short time frame, because the orbital period of the star is much longer than the time covered by the available data (see subsection 7.7). Another possible reason is that the spectra were recorded approximately at intervals of the actual period. When

Name	$T_{\text{eff}}[K]$	$\log g [\frac{cm}{s^2}]$	$[\log \frac{n_{He}}{n_H}]$	$\log p$
SdB				
J094750.71+162731.7	27850 ± 150	5.638 ± 0.028	-2.1 ± 0.04	-97.62
J133040.91-001710.7	27440±50	5.631 ± 0.008	-2.536± 0.300	-86.94
J222732.67+223610.2	31330 ± 95	5.773 ± 0.012	-2.023 ± 0.018	-30.22
J162344.84+122913.1	27070 ± 60	5.428 ± 0.008	-3.1 ± 0.06	-29.84
J134947.71+250811.0	28011 ± 7	5.5968 ± 0.012	-2.87 ± 0.04	-28.56
J200358.60-113129.1	30000 ± 600	5.63 ± 0.11	-2.74 ± 0.17	-24.36
J173057.93+320737.0	26650 ± 80	5.444 ± 0.014	-2.65 ± 0.26	-16.80
J142741.03+014254.9	28730 ± 90	5.538 ± 0.014	-3.42 ± 0.08	-15.84
J163644.53+251644.9	28950 ± 220	5.72 ± 0.04	-2.64 ± 0.09	-14.04
J170116.02+240351.5	28050 ± 350	5.57 ± 0.05	-2.59 ± 0.1	-11.18
J173410.96+084753.0	29900 ± 600	5.69 ± 0.09	-2.23 ± 0.11	-11.01
J072245.26+305233.4	24196 ± 36	5.302 ± 0.75	-2.45 ± 0.06	-10.58
J081204.81+135204.6	26500 ± 80	5.325 ± 0.013	-2.80 ± 0.06	-10.47
J073225.83+153729.7	25760 ± 165	5.484 ± 0.023	-2.74 ± 0.09	-9.66
J094729.36+271627.0	29150 ± 140	5.670 ± 0.023	-2.81 ± 0.05	-8.85
J072614.68+415748.9	28500 ± 60	5.556 ± 0.013	-2.64 ± 0.04	-7.97
J163557.64+341427.1	28650 ± 190	5.69 ± 0.04	-2.86 ± 0.08	-6.35
J074852.07+454903.8	27200 ± 55	5.537 ± 0.009	-2.39 ± 0.012	-5.80
J080738.96-083322.6	26420 ± 270	5.422 ± 0.025	-2.49 ± 0.04	-5.80
J081342.92+275034.7	26340 ± 80	5.508 ± 0.012	-2.69 ± 0.04	-5.79
J111621.61+390254.3	26650 ± 145	5.471 ± 0.023	-1.98 ± 0.04	-5.40
J121735.90+375824.9	27750 ± 85	5.170 ± 0.012	-2.72 ± 0.04	-5.15
J071424.12+401645.8	27300 ± 400	5.52 ± 0.07	-2.71 ± 0.10	-4.32
J082159.06+411228.0	25800 ± 130	5.423 ± 0.019	-2.42 ± 0.05	-4.32
SdOB				
J183317.73+642737.1	36700 ± 400	5.98 ± 0.05	2.55 ± 0.01	-106.66
J064916.11+383419.7	33663 ± 0.11	5.716 ± 0.007	-1.9 ± 0.008	-59.75
J012855.43+401048.6	33350 ± 250	6.06 ± 0.05	-1.69 ± 0.05	-5.74
J090318.36+043533.7	38050 ± 170	5.818 ± 0.018	-3.44 ± 0.13	-5.33
J144737.75+020942.5	32440 ± 305	5.68 ± 0.05	-2.70 ± 0.15	-5.14
sdO				
J092520.01+273619.7	40400 ± 550	5.60 ± 0.06	-2.35 ± 0.09	-6.48
BHB				
J164501.90+415113.2	18540 ± 110	4.511 ± 0.016	-1.71 ± 0.04	-19.22
J125410.86-010408.3	21540 ± 125	4.985 ± 0.001	-1.63 ± 0.022	-5.96
J083334.76-045759.3	20240 ± 235	5.571 ± 0.027	-4.00 ± 0.75	-4.62
J162928.33+275912.0	17950 ± 105	4.322 ± 0.016	-2.21 ± 0.026	-4.47

pre-ELM WD				
J112157.13+605210.4	11657 ± 30	5.459 ± 0.012	-3.3 ± 0.9	-32.70
J142421.30-021425.4	12272 ± 115	5.646 ± 0.038	-5.1 ± 1.2	-21.41
J112914.16+471501.7	11640 ± 75	5.398 ± 0.026	-5.1 ± 1.3	-5.09

Table 1: Radial velocity variable subdwarfs, which were not identified as RV variable before. The atmospheric parameters T_{eff} , $\log g$ and helium to hydrogen abundance ratio $\log(\frac{n_{\text{He}}}{n_{\text{H}}})$ are also given as well as the determined $\log p$ value.

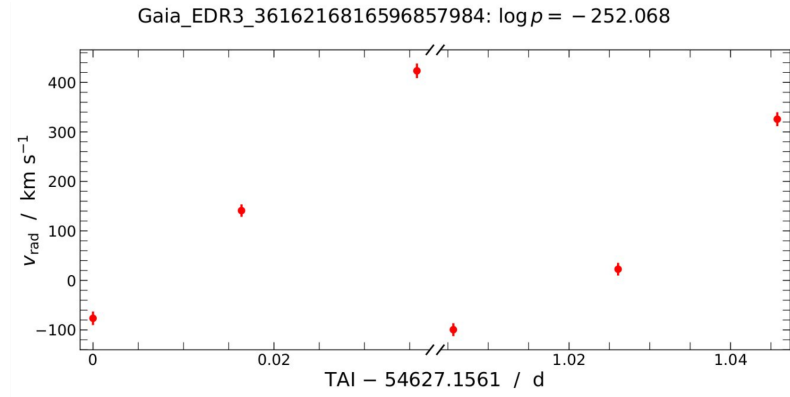


Figure 7.3: Radial velocity plotted over international atomic time for SDSS J140118.80-081722.6. It is a highly significant detection, because its $\log p$ is -252, far below the detection limit.

the number of candidates for radial velocity variability is added to the number of detections (in total 97), the fraction becomes to 8.9 %. An example for a star, which has already been detected as a variable one by Kupfer et al. (2015), is SDSS J150829.02+494050.9. However, it is classified as a candidate for radial velocity variability in this study (see Table 7). The reason is, that the different spectra are approximately recorded after a multiple of one period, which is 0.97 d for this star (Kupfer et al.; 2015). This behaviour can be seen by its RV curve (shown in Figure 7.5).

The most interesting object in this study is the highly variable, extreme He-sdOB SDSS J183317.73+642737.1, as only very few RV variables are known among He-sdOB stars. This star is discussed in more detail in subsection 7.4.

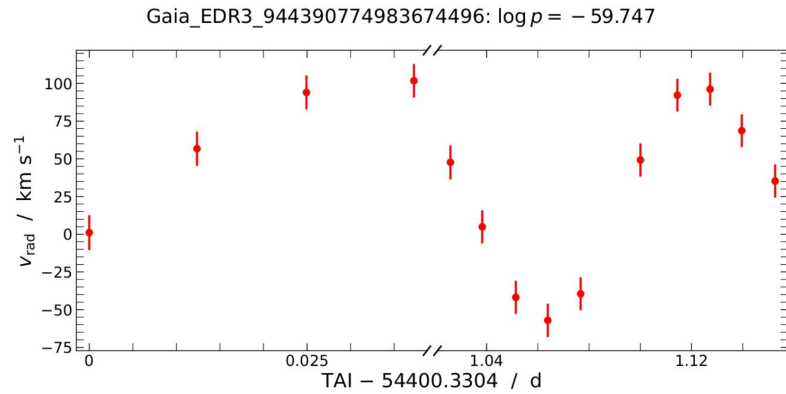


Figure 7.4: Radial velocity plotted over international atomic time for SDSS J064916.11+383419.7. It's a detected RV variable, because its $\log p$ is < -4 .

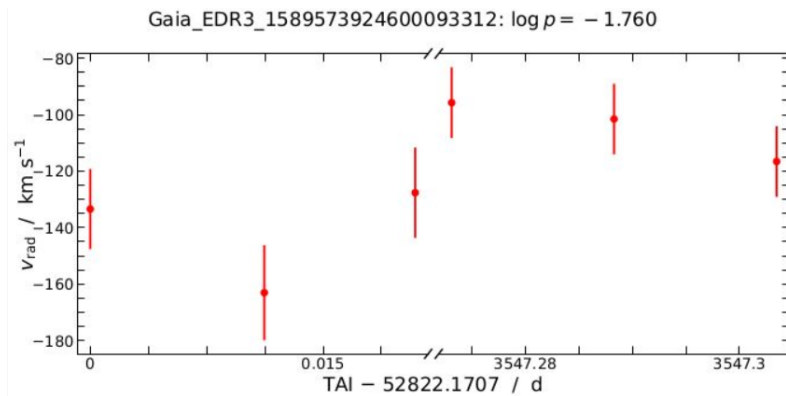


Figure 7.5: Radial velocity plotted over international atomic time for SDSS J150829.02+494050.9. It is a candidate for RV variability, because its $\log p$ is in the range -4 and -1.3 .

7.3 Kiel-diagram

The sample allowed to study the radial velocity of stars dependent on their atmospheric parameters, like T_{eff} and $\log g$, and thus dependent on their spectral class and evolutionary stages. Figure 7.6 exhibits the distribution of the full sample in the Kiel-diagram, where $\log g$ is visualised over T_{eff} .

The stars of the sample cluster at different positions in the Kiel-diagram. The different populations of stars are marked in Figure 7.6. Between the sdBs and BHBs, a gap at around 22000 K can be found. This gap was found before by Newell and Graham (1976). Hence, the term "Newell gap" has coined (Heber; 1992). This gap suggests that for different types of stars, different evolution processes are likely, because the morphology of the horizontal branch evolutionary tracks changes near

the gap temperature of 22000 K from evolution at constant T_{eff} to lower gravity for cooler stars to blueward evolution at roughly constant gravity for the hotter ones (Heber; 1992). Evolutionary tracks, taken from (Dorman et al.; 1993), for different masses are implemented in Figure 7.7.

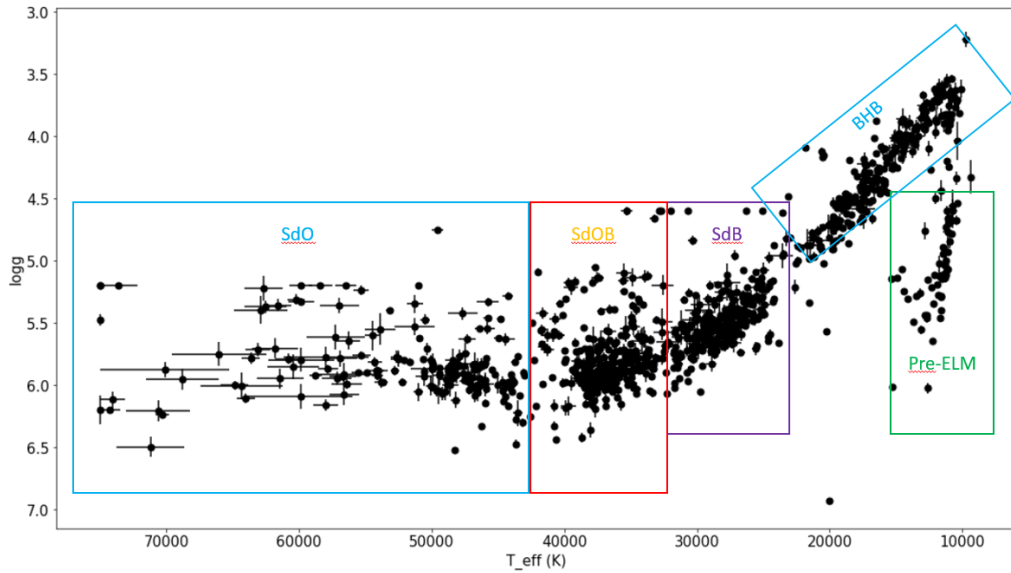


Figure 7.6: Distribution of the stars in the Kiel-diagram, where $\log g$ is plotted over the effective temperature. Error bars consider statistical uncertainties only.

In Figure 7.7 the same diagram like in Figure 7.6 shown, but stars, which were detected to be variable, and also those, which were determined to be candidates for RV variability, are marked. The blue dots show the variable stars, while the red ones show the candidates. The dots colored in light grey are stars that show no sign to be variable. As can be seen in Figure 7.7, the distribution of RV variable stars for different populations looks quite inhomogeneous. Only one variable star is located in the region of sdO stars. Five variable stars are located in the region of sdOB stars, but most RV variable stars, are sdB stars. The fractions for variable stars in each population is specified in Table 7.6. The distribution of variable stars in the Kiel diagram can even be seen more clearly in Figure 7.8, where only the detected variables are marked in blue, while all other stars are colored in light grey. The distribution of candidates for RV variability in the Kiel diagram is shown in Figure 9.1 in the appendix, where only the candidates are marked in red, while all other stars are colored in light grey.

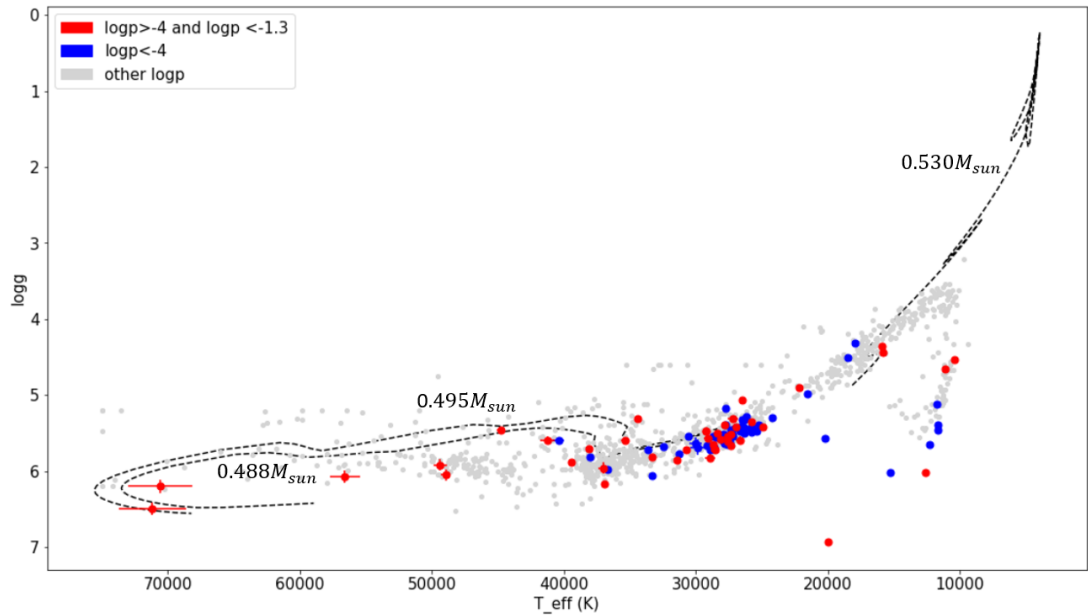


Figure 7.7: Distribution of detections of variable stars (blue), candidates for variability (red) and stars which show no sign of variability (light grey) in the Kiel diagram. The tracks (Dorman et al.; 1993) are shown with dashed lines, labeled with their masses.

7.4 SDSS J183317.73+642737.1

The most interesting and peculiar hot subdwarf, detected to be in a binary, in this thesis, is SDSS J183317.73+642737.1. The special property of SDSS J183317.73+642737.1 is its extremely high helium abundance, so it is classified as helium rich variable sdOB. The helium to hydrogen abundance ratio ($\log(\frac{n(He)}{n(H)})$) for SDSS J183317.73+642737.1 is 2.55 ± 0.01 . Its atmosphere consists almost entirely of helium. This star had to be fitted separately with an additional grid for helium rich subdwarfs, because the first fit ended up at the upper limit of the helium abundance of the standard grids. All stars, where the fit ended up at this border are listed in Table 9 in the appendix. In the fitted spectra (one example spectrum is shown in Figure 7.9) the helium I and helium II lines can be seen very clearly, while the Balmer lines are completely absent in the spectra. The different absorption lines are marked in the spectrum.

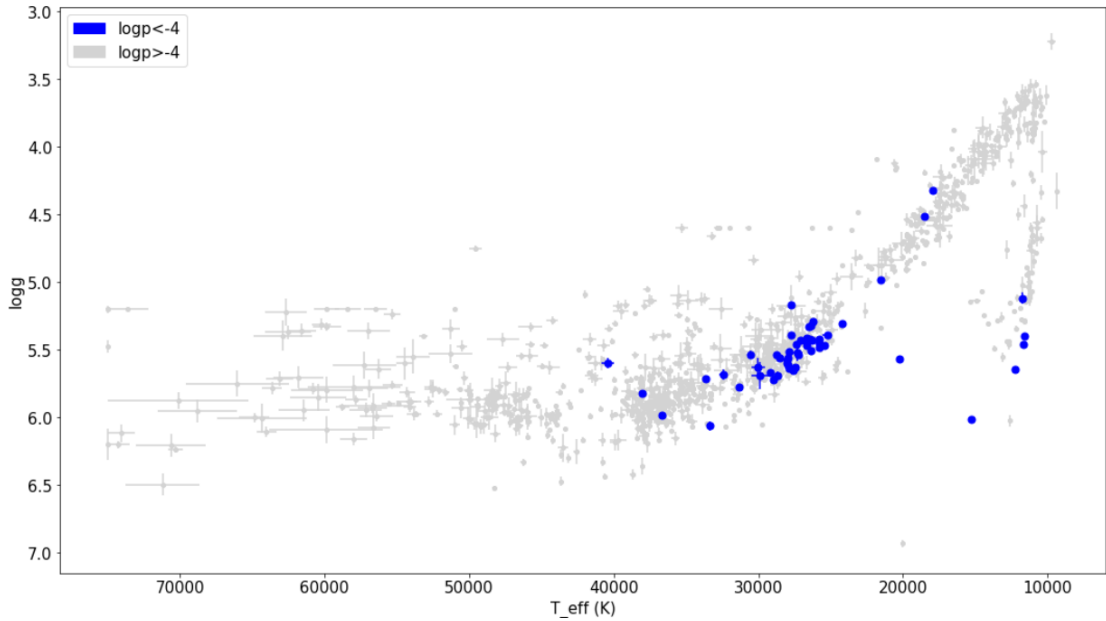


Figure 7.8: Distribution of variable stars in the Kiel diagram (marked in blue), where the candidates and the stars, that show no variability are colored in light grey.

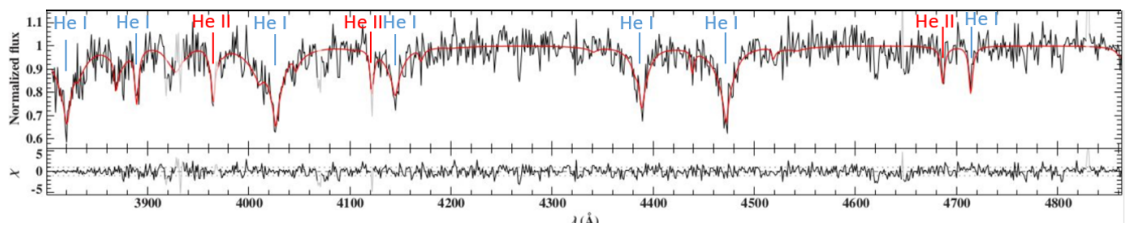


Figure 7.9: Fitted spectrum for the extreme helium-rich variable star SDSS J183317.73+642737.1. The helium I and helium II lines are marked in blue and red, respectively. Note the absence of hydrogen Balmer lines. The red line is the best fit of the synthetic spectrum.

The corresponding change of the radial velocity over time, is shown in Figure 7.10. Another unusual atmospheric feature of SDSS J183317.73+642737.1 is its temperature. The temperatures for extremely helium rich sdOBs or sdOs is, normally, more than 38000K. The temperature for this one is considerably lower 36600 ± 400 K, which would be typical for an intermediate helium rich or an hydrogen rich sdOB. To understand how and under which conditions SDSS J183317.73+642737.1 evolved, it is very important to find out how long the orbital period of this binary and which type of star its companion is. It could allow an important test of the different evolution scenarios of subdwarfs. However, this is not possible with the SDSS data of this thesis, as there are too few spectra with too short intervals, to determine the period of the binary. It is also not possible to derive the type of companion by the spectra, so that follow-up observations are necessary.

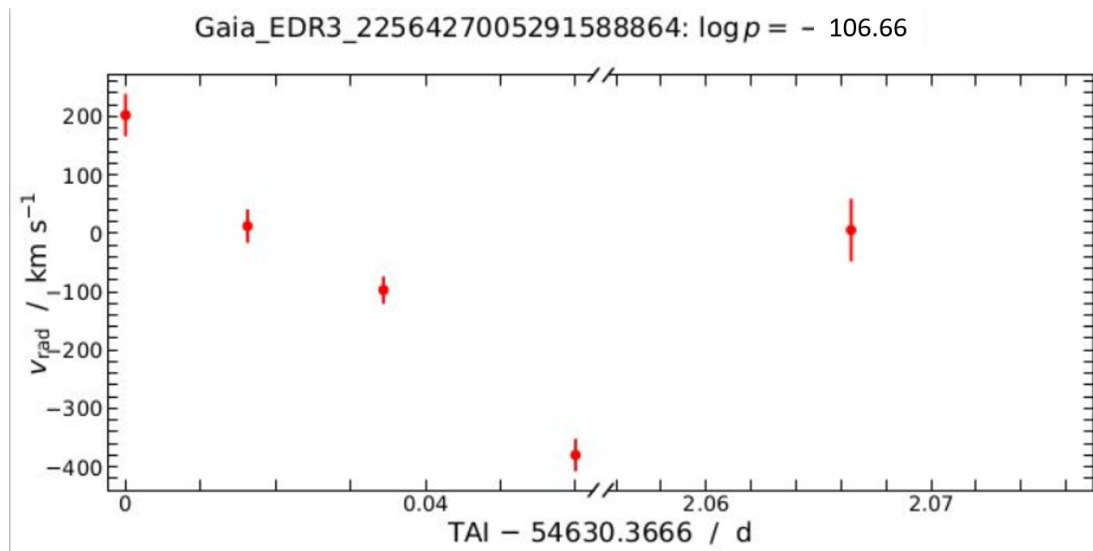


Figure 7.10: Radial velocity plotted over international atomic time for the extreme helium rich SDSS J183317.73+642737.1. It is detected as variable, because its $\log p$ is < -4 .

7.5 Radial velocity variability depending on helium abundance

Besides of spectral classes, the RV variability fractions of stars with different helium abundances can be derived. Figure 7.11 shows a $T_{\text{eff}} - \log(\frac{n(\text{He})}{n(\text{H})})$ -diagram of the whole sample, allowing for an analysis of the impact of helium abundances on subdwarf variability. To better categorize the findings, the classes of helium poor ($\log(\frac{n(\text{He})}{n(\text{H})}) < -1$), intermediate-helium ($-1 < \log(\frac{n(\text{He})}{n(\text{H})}) < 0.6$) and helium rich ($\log(\frac{n(\text{He})}{n(\text{H})}) > 0.6$) subdwarfs were adopted from Geier et al. (2022). To visualise the different categories of helium abundances, horizontal dashed lines are implemented in the Figure 7.11.

The grid border of helium-rich stars was at $\log(\frac{n(\text{He})}{n(\text{H})}) = 1$, so no star has a higher helium abundance in the figure, but that doesn't mean, that it really has no higher helium abundance. All stars which run against the upper limit for helium abundances are listed in Table 9 in the appendix. The helium rich variable star SDSS J183317.73+642737.1, for example, was re-fitted individually with a different grid and it turned out to have a helium to hydrogen abundance ratio of $\log(\frac{n(\text{He})}{n(\text{H})}) = 2.55 \pm 0.01$ (see subsection 7.4). The same diagram like in Figure 7.11 can also be seen in the appendix, where in Figure 9.2 only the detected variable objects and in Figure 9.3 only the candidates are depicted. What also emerges from Figure 7.11 are the different helium abundances by every population. There are no intermediate-helium or helium-rich stars among the sdBs or BHB stars. The sdOBs sprinkle in any of those groups, but only a few are helium-rich, like the variable star SDSS J183317.73+642737.1, which makes it even more special. Many of the sdOs are helium-rich. The difference in RV-variability of helium poor and helium rich subdwarfs is striking. In total SDSS J183317.73+642737.1 is the only variable star in the group of helium rich stars. Furthermore no intermediate helium star was detected to be variable. 2 candidates are in the region of helium-rich and 5 in the region of intermediate helium stars. The fractions of detections in relation to the number of candidates and stars with no variations are shown in Table 2.

Helium-abundance	Detections	Candidates	No variations	Fraction[%]
Helium-rich	1	2	115	0.85
Intermediate-helium	0	5	112	0
Helium-poor	52	37	771	6.4
Sum	53	44	998	5.1

Table 2: Number of detected variable stars, candidates and stars with no variations in the different helium abundance-groups. Therefore the fraction of detections is given.

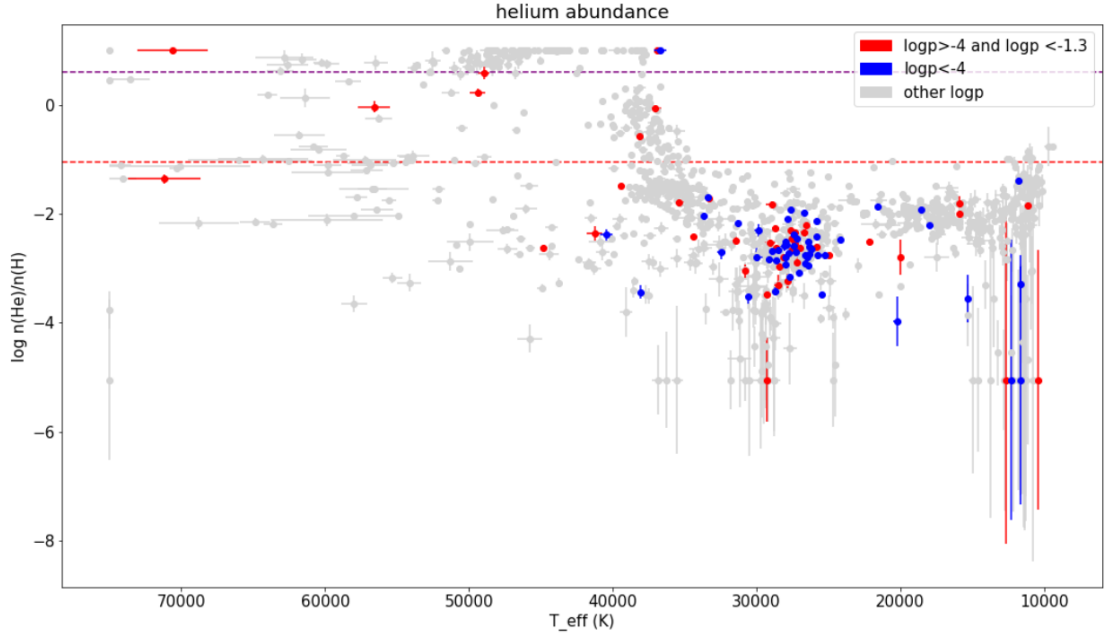


Figure 7.11: Distribution of stars by helium abundance. The stars, detected as variables, are marked in blue, candidates in red and stars with no variability marked in light grey. To characterize the different groups of helium abundances, two dashed horizontal lines are inserted. The red one splits the helium poor from the intermediate helium ones and the magenta one splits the group of intermediate helium stars from the group of extremely helium rich stars. Note that the upper grid limit for the helium abundance is at $\log\left(\frac{n(\text{He})}{n(\text{H})}\right)=1$. Therefore, extremely helium rich stars pile up at this abundance. The only RV variable He-sdO star SDSS J183317.73+642737.1 (see subsection 7.4) is the coolest of those.

The highest fraction of detections can be found in the group of helium-poor stars, mainly sdB stars. While the helium poor stars have a variability fraction of 6.4%, the variability fractions for intermediate helium stars is 0% and for helium rich stars 0.85%. To clarify where all variable stars lie in the Kiel-diagram, with their helium abundances stand out with different colors Figure 7.12 is depicted. Magenta is for helium-rich stars, red is for intermediate-helium ones and blue are the helium-poor ones. This figure shows more clearly, how the variability of a star depends on its helium abundance, and how the helium abundance depends on the temperature or the position in the Kiel diagram. The same figure, like Figure 7.12, but for the candidates is shown in the appendix (Figure 9.4).

Table 3 shows the number of stars with different helium abundances in the sample and the fraction to the number of total stars contained in the sample. The highest

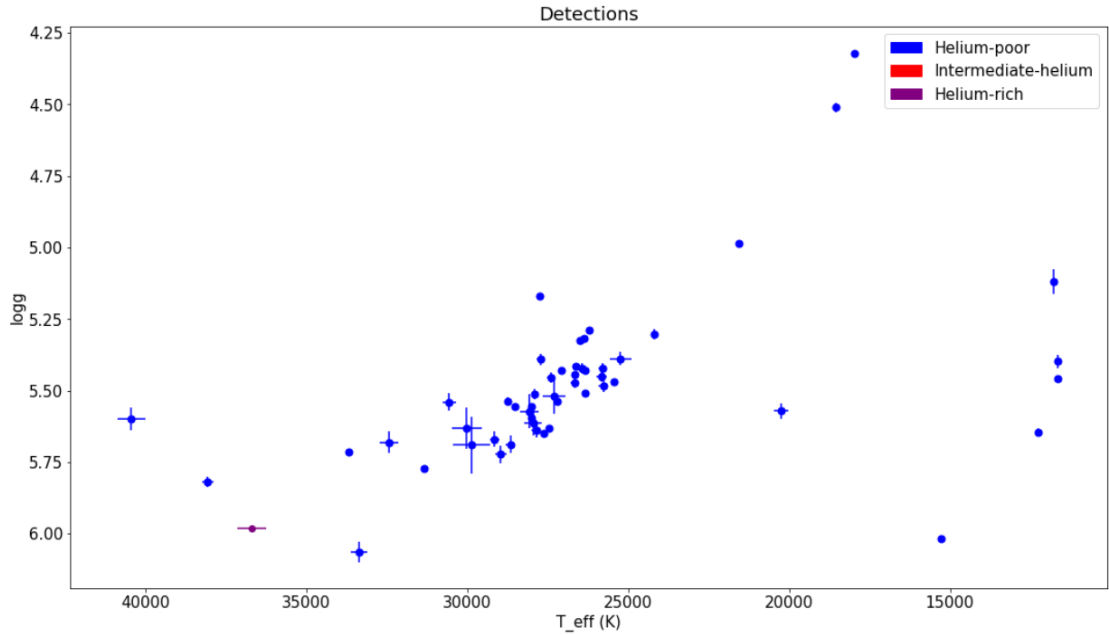


Figure 7.12: Detections of variable subdwarfs in the Kiel-diagram. The hydrogen rich stars are marked in blue, the only He-rich one in magenta.

fraction, in this sample, are helium-poor stars. The intermediate helium and helium rich stars have almost the same fraction at around 10.75%.

helium-abundance	number of stars	Fraction to number of total stars[%]
Helium-rich	118	10.8
Intermediate-helium	117	10.7
helium-poor	860	78.5

Table 3: Number of stars in each category. Therefore the fraction in relation to the number of total stars is given.

7.6 Radial velocity variability fractions by spectral type

The different populations of stars in the sample were divided into five main groups: SdOs, sdOBs, sdBs, BHBs and pre-ELM WDs. Those different populations were extracted by separating the clusters (shown in Figure 7.6) from each other. The different populations with the number of detections, candidates and stars with no variations are listed in Table 4. Therefore the sdOBs are divided into helium rich, intermediate helium and helium poor sdOBs, as they sprinkle in every category of helium abundances. Breaking down the observed variations into groups, reveals

Type	Detections	Candidates	No Variation	Fraction [%]
sdO	1	7	203	0.48
Heliumrich sdOB	1	1	12	8.3
Intermediate helium sdOB	0	2	75	0
Heliumpoor sdOB	4	4	188	2.1
sdB	38	23	226	15.2
BHB	4	4	248	1.6
pre-ELM WD	5	3	46	10.2
sum	53	44	998	4.8

Table 4: Number of detected variables, candidates and stars with no variations for the different populations in the sample of this thesis. Therefore the fraction of detections was calculated.

clear differences between the different classes. The fractions of detections for sdBs (15.2%) and pre-ELM WDs (10.2%), are significantly higher than among the other groups. The fraction of intermediate helium variable sdOB (8.3%) seems to be almost as high as for sdBs or pre-ELM WDs. But this might be a coincidence, as only 14 stars in total are in this group, while one was detected as a variable one.

7.7 Time distribution of observed data

The fractions of detected variables are less than determined by Geier et al. (2022), especially for sdB stars. The detectability of variable stars is restricted by different reasons, like the observational timespan over which they are observed and the distribution of known binaries as a function of their period (Kupfer et al.; 2015), as well as the height of the amplitude of the RV curve. Since the SDSS observations often have short observation intervals and few epochs of observations, long period binaries have almost no chance of being detected. The number of stars, depending on the timespan between first and last observation is displayed in Figure 7.13, on a logarithmic scale in a histogram. Three main groups stand out. The largest group has observation intervals of less than 2.5h. Those stars were observed three to five times in a row by the SDSS. In this group only 4 stars out of 604 were detected as variables. This corresponds to a fraction of 0.7%. Another group stands out for $1d < t < 100d$. For those, at least, two observational epochs were recorded. In this group 28 stars out of 295 were detected as variables, which corresponds to a fraction of 9.5%. The last group has observational timespans with $t > 100d$ and consists stars that were observed in SDSS I and II, as well as in SDSS III. In this group 21 out of 196 were detected as variables. This group has the highest fraction for detections, of 10.7%. The intervals of available observations have a strong

impact on the detection probability. This statistic suggests, that there should be many more variable stars in the sample, which could not be detected, because the observational intervals of the star is too short.

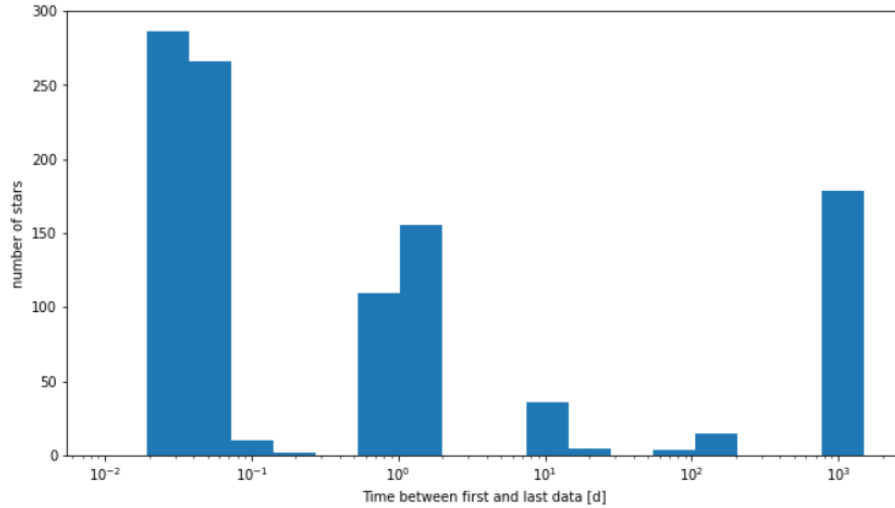


Figure 7.13: Histogram of the distribution of the timespan between the first and last data of a star provided by the SDSS.

7.8 Comparison with Mattig

Parallel to this thesis, Mattig (2022) also conducted a radial velocity study of the same sample of stars like in this thesis. In contrast to this thesis, Mattig (2022) used the same spectra as in this thesis, but matched the blue and red part together afterwards. Therefore Mattig (2022) calculated the radial velocity for every selected absorption line, like the Balmer series or helium lines. Mattig (2022) determined the radial velocity by calculating the mean value and the standard derivation of those lines. Mattig (2022) assumed the absorption lines by combining Doppler and a Lorentzian profile. With this method, Mattig (2022) was not able to determine atmospherical parameters. The atmospherical parameters of Mattig (2022) are taken from literature, if available. For more details, see section 4 in Mattig (2022). The results of Mattig (2022) are compared with the results of this thesis in this section.

Significant differences between the results of the analysis of Mattig (2022) and this thesis appear. To give an overview over the different number of detections and candidates, Table 5 is added.

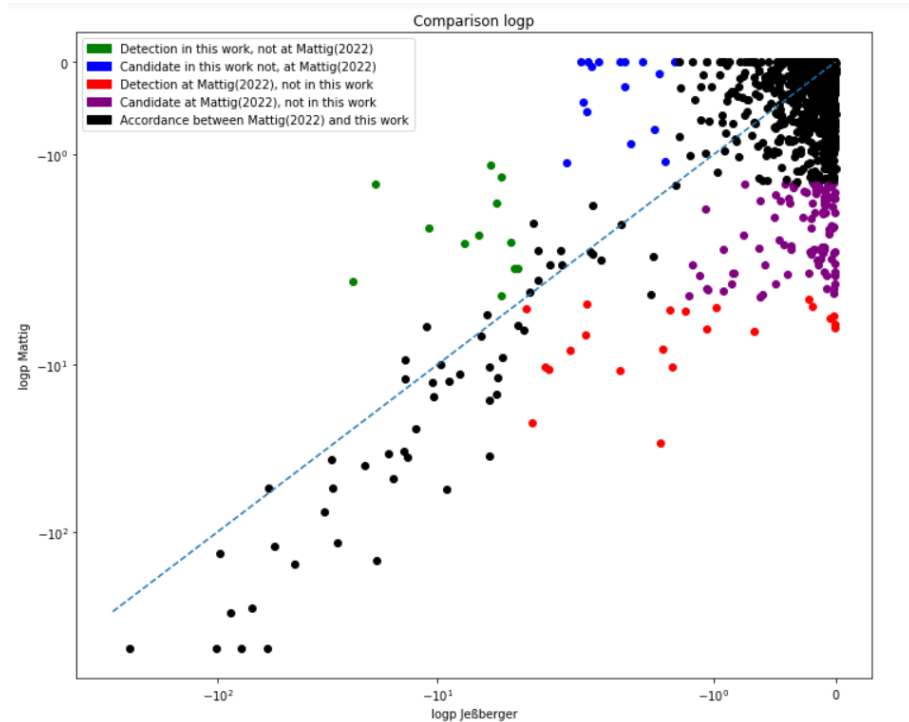


Figure 7.14: Distribution of $\log p$ values in Mattig (2022) and this thesis. Stars marked in green and blue were detections/candidates in this thesis but not in Mattig (2022). Stars marked in red and magenta were detections/candidates in Mattig (2022) but not in this thesis. The black points describe the stars, where the results from Mattig (2022) match the results of this thesis. The dashed diagonal line illustrates, where the $\log p$ values of the works would be equal.

(Mattig; 2022) detected 27 more stars as variables and more than three times more candidates, than detected, in this thesis. This can be explained by two main reasons. On one hand, the number of total stars differ by 129, because Mattig (2022) did not sort out all the stars, where the spectral fit ended up at the upper limit for the surface gravity ($\log g=6.6$, see subsection 6.1). On the other hand, the calculation of the $\log p$ value of Mattig (2022) was different to the calculation of this thesis, because Mattig (2022) assumed no systematic error, while in this thesis a systematic error of $10 \frac{\text{km}}{\text{s}}$, was added (see Equation 6.2). This causes in average lower $\log p$ values of Mattig (2022) compared to this thesis, so that some stars were detected as variables at Mattig (2022) but not in this thesis (in total 23). There are also 12 stars, which were detected as variables in this thesis but not in Mattig (2022). The candidates follow the same scheme. The distribution and comparison of $\log p$ values of Mattig (2022) with this thesis is shown in Figure 7.14. For illustration a diagonal line is displayed. Stars, that lie under the line have lower

	(Mattig; 2022)	This thesis
detections	80	53
candidates	153	44
no variations	991	998
total stars	1224	1095

Table 5: Comparison between (Mattig; 2022) and this thesis.

$\log p$ values at Mattig (2022) and vice versa. In total 334 stars have a lower $\log p$ value in this thesis, while 761 stars have a lower $\log p$ value in Mattig (2022). The latter is most likely due to the neglect of any systematic uncertainties by Mattig (2022).

The comparison of detected variables with different spectral types, is shown in Table 6. The fractions for different spectral types are similar and show an approximate accordance between the studies, except for pre-ELM WDs, as Mattig (2022) classified them as unclassified stars, as well as BHBs. Mattig (2022) did not classify any stars in the sample as pre-ELM WDs or BHBs. The fractions of detected variable sdO and sdOB stars, were higher at Mattig (2022) and lower for sdB stars, because Mattig (2022) classified some stars as sdB stars, which are classified as BHB stars in this thesis, so that a higher number of stars are classified as sdB stars by Mattig (2022).

Type	This thesis	Mattig	fraction this thesis [%]	fraction Mattig [%]
sdO	1	3	0.48	1.8
sdOB	5	7	1.7	3.7
sdB	38	61	15.2	11.6
BHB	4	0	1.6	0
pre-ELM WD	5	0	10.2	0
unclassified	0	9	0	3

Table 6: Comparison of number of detected variables by Mattig (2022) and this thesis.

8 Summary and outlook

The stellar population of hot subdwarfs contains important informations to understand stellar binary evolution. Subdwarf binaries are known to have periods of 1 h up to 30 days, with a maximum at around one day, but only 5% of all binaries have a period shorter than 2.5 h (Kupfer et al.; 2015). The sample consists of a total number of 2048, mainly hot subdwarfs of type sdB, sdO and sdOB as well as blue horizontal branch stars (BHB) and progenitors of white dwarfs (WD) of extremely low mass ($\sim 0.2M_{\odot}$) (pre-ELM WD). The SDSS provides the blue part of spectra of that sample. Geier et al. (2022) already comprehensively analyzed 646 stars. Many of them were in the sample analyzed in this thesis. Their results suggested dependencies of binary evolution and spectral classes, as well as helium abundances. This thesis extends the previous study by Geier et al. (2022) substantially, and makes it the largest study of radial velocity variability of hot subdwarfs, yet.

All classes of stars (subdwarfs, BHBs and pre-ELM WDs) were analyzed in a study of their radial velocity variability. 817 stars were sorted out, because it was impossible to analyze their spectra, due to their very low signal to noise ratio. Further 136 stars were misclassified before and turned out to be high gravity objects rather than subdwarfs. Therefore, they were excluded from further analysis. The spectra of the remaining 1095 stars were fitted with a grid-based global fitting method, developed by Irrgang et al. (2014), that facilitates quick and precise determinations of atmospheric parameters (T_{eff} , $\log g$ and helium to hydrogen abundance ratio $\frac{n(\text{He})}{n(\text{H})}$) and radial velocities. For each star at least 3 (up to 25) spectra taken to different times are available. This allows to search for radial velocity variations indicative of binarity. The false detection probability p was calculated and a star was considered to be variable if the false detection probability is less than 10^{-4} ($\log p < -4$), and possibly variable if p is between 5^{-2} and 10^{-4} . This allowed to study RV-variability as a function of the location in the $T_{\text{eff}}\text{-}\log g$ and $T_{\text{eff}}\text{-}\log(\frac{n(\text{He})}{n(\text{H})})$ diagrams. The stars were assigned to their spectral classes by their characteristic properties. All stars with higher temperatures than 40000 K belong to the group of sdO stars. The sdOB stars have temperatures between 32000 K and 40000 K. The sdBs are at temperatures between 20000 K and 32000 K. Stars with temperatures at around 11000-12000 K and $\log g$ between 4.5 and 5.7 were assigned to the group of pre-ELM WDs. The stars cooler than 21000 K and with lower $\log g$ -values than the pre-ELM WDs are BHBs. Furthermore the helium abundances of stars were divided into 3 regions. Helium poor stars, where the helium to hydrogen abundance ratio is smaller than solar ($< \log(\frac{n(\text{He})}{n(\text{H})}) = -1$). Intermediate helium stars, where the helium to hydrogen abundance ratio is between solar helium and

$\log\left(\frac{n(\text{He})}{n(\text{H})}\right)=0.6$). Helium rich stars for an even higher helium to hydrogen abundance ratio.

Summarizing the results of this thesis allows to draw several conclusions :

- The observational timespan has a huge impact on the detection probability of variables: Only 0.7% of stars with observational data shorter than 2.5 h, were detected as variables. For an observational time between 1-100d 28 stars were found to be variable (9.5%). 21 stars out of 196 showed radial velocity variability, where the observational timespan was longer than 100d. This corresponds to a fraction of 10.7%. This leads to the conclusion, that it is more likely to find variables, for longer observational timespans.
- Most of the sdBs are hydrogen rich, while many of sdOs are helium rich. SdOBs sprinkle in every region of helium abundances. In the sample only hydrogen rich sdBs were found, while almost the half of all sdOs are helium rich or have intermediate helium. 188 out of 287 sdOBs are hydrogen rich and 77 have intermediate helium, while 14 are helium rich. This suggests that the different types of sdOBs evolve in different ways.
- In the $T_{\text{eff}}\text{-log } g$, the so called "Newell gap", between the population of sdBs and BHBs at around 22000 K is confirmed. This can be attributed to the fact, that the morphology of the horizontal branch evolutionary tracks changes near the gap temperature of 22000 K (Dorman et al.; 1993).
- The distribution in the Kiel diagram matches the evolutionary models of BHBs, but a clear division between the sdBs and sdOBs appears, at a temperature of ~ 32000 K.
- pre-ELM WDs are limited to small temperatures ranges, which suggests that they have very small masses.
- Most helium rich subdwarfs are single stars. Among extreme helium subdwarfs one was detected as variable, while no intermediate helium variable star was found. This strengthens previous results of Geier et al. (2022).
- The different behavior of helium poor and helium rich hot subdwarfs, indicates that they are very unlikely to be related in evolutionary scenarios. While 52 helium poor variable stars were found, only one helium rich star was detected as variable. This leads to the conclusion that helium poor and helium rich subdwarfs are not related
- Just like for helium rich and helium poor stars, sdO and sdB stars show significantly different behaviors. Only one sdO star, which corresponds to a

fraction of 0.48% showed radial velocity variability, while 15.2% of all sdBs showed this behavior (38 sdBs). So it seems that subdwarfs of type O and B are not related.

- The fractions for RV variable hydrogen rich sdOBs is much lower than for sdBs. In total only 4 hydrogen rich sdOs are found in a binary (2.1%), while a much higher fraction of sdBs (15.2%) were detected as variable. That leads to the conclusion, that most sdOBs do not evolve in a binary.
- pre-ELM WDs often reside in binaries: 5 out of 54 pre ELMs, which is a fraction of 10.2%, reside in a binary. This is a nearly as high fraction as for sdBs. It might be that pre-ELM WDs have a similar evolution scenario as sdBs.

The results of this thesis open up a number of possibilities for different studies and observations. Since the resolution of spectra provided by the SDSS is limited and more than 50% of the stars in the sample were observed for short timespans of less than 2.5h, follow up studies with high resolution spectra and longer observation time are needed to estimate the true fraction of variable subdwarfs and their distribution in the parameter space discussed in this thesis. Only 5% of all detected sdB binaries have a period shorter than 2.5h, what suggests that an observation time of less than 2.5h is not effective for finding binaries.

The stars, where the fit ended up at the upper limit of the helium abundance, need to be re-investigated with a different grid, to determine their atmospheric parameters.

Follow up observations for the detected RV variable objects are needed to derive orbital parameters, like their period, amplitude and eccentricity and determine their mass as well as the type of companion.

The most interesting follow up study and observation can be carried out for the only helium rich variable star SDSS J183317.73+642737.1, which can lead to a better understanding of the different evolutionary scenarios of hot subdwarfs and stars in general.

References

- Calcaferro, L. M., Althaus, L. G. and Córscico, A. H. (2018). The coolest extremely low-mass white dwarfs, *Astronomy & Astrophysics* **614**: A49.
- Copperwheat, C., Morales-Rueda, L., Marsh, T., Maxted, P. and Heber, U. (2011). Radial-velocity measurements of subdwarf b stars, *Monthly Notices of the Royal Astronomical Society* **415**(2): 1381–1395.
- Dorman, B., Rood, R. T. and O’Connell, R. W. (1993). Ultraviolet radiation from evolved stellar populations. i. models, *The Astrophysical Journal* **419**: 596.
- El-Badry, K., Rix, H.-W., Quataert, E., Kupfer, T. and Shen, K. J. (2021). Birth of the elms: a ztf survey for evolved cataclysmic variables turning into extremely low-mass white dwarfs, *Monthly Notices of the Royal Astronomical Society* **508**(3): 4106–4139.
- Fukugita, M., Shimasaku, K., Ichikawa, T., Gunn, J. et al. (1996). The sloan digital sky survey photometric system, *Technical report*, SCAN-9601313.
- Geier, S. (2015). Heiße unterzwerge, *Spektrum der Wissenschaft* .
- Geier, S. (2020). The population of hot subdwarf stars studied with gaia-iii. catalogue of known hot subdwarf stars: Data release 2, *Astronomy & Astrophysics* **635**: A193.
- Geier, S., Dorsch, M., Pelisoli, I., Reindl, N., Heber, U. and Irrgang, A. (2022). Radial velocity variability and the evolution of hot subdwarf stars, *Astronomy & Astrophysics* **661**: A113.
- Geier, S. et al. (2011a). Binaries discovered by the muchfuss project: Sdss j08205+0008—an eclipsing subdwarf b binary with a brown dwarf companion, *The Astrophysical Journal Letters* **731**(2): L22.
- Geier, S. et al. (2011b). The muchfuss project—searching for hot subdwarf binaries with massive unseen companions—survey, target selection and atmospheric parameters, *Astronomy & Astrophysics* **530**: A28.
- Green, R. F., Schmidt, M. and Liebert, J. (1986). The palomar-green catalog of ultraviolet-excess stellar objects, *The Astrophysical Journal Supplement Series* **61**: 305–352.
- Gunn, J., Carr, M., Rockosi, C., Sekiguchi, M., Berry, K., Elms, B., De Haas, E., Ivezić, Ž., Knapp, G., Lupton, R. et al. (1998). The sloan digital sky survey photometric camera, *The Astronomical Journal* **116**(6): 3040.
- Gunn, J. E., Siegmund, W. A., Mannery, E. J., Owen, R. E., Hull, C. L., Leger, R. F., Carey, L. N., Knapp, G. R., York, D. G., Boroski, W. N. et al. (2006). The 2.5 m telescope of the sloan digital sky survey, *The Astronomical Journal* **131**(4): 2332.

- Han, Z.-w., Podsiadlowski, P., Maxted, P. F. and Marsh, T. R. (2003). The origin of subdwarf b stars—ii, *Monthly Notices of the Royal Astronomical Society* **341**(2): 669–691.
- Heber, U. (1992). Hot subluminoous stars, *The Atmospheres of Early-Type Stars*, Springer, pp. 231–246.
- Heber, U. (2009). Hot subdwarf stars, *Annual review of Astronomy and Astrophysics* **47**: 211–251.
- Heber, U. (2016). Hot subluminoous stars, *Publications of the Astronomical Society of the Pacific* **128**(966): 082001.
- Heber, U. (2017). Stripped red giants-helium core white dwarf progenitors and their sdb siblings, *20th European White Dwarf Workshop*, Vol. 509, p. 85.
- Heber, U., Edelmann, H., Lisker, T. and Napiwotzki, R. (2003). Discovery of a helium-core white dwarf progenitor, *Astronomy & Astrophysics* **411**(3): L477–L480.
- <http://classic.sdss.org/legacy/index.html> (2014).
URL: <http://classic.sdss.org/legacy/index.html>
- <https://classic.sdss.org/dr7/instruments/spectrographs/index.html> (2003).
URL: <https://classic.sdss.org/dr7/instruments/spectrographs/index.html>
- <https://commons.wikimedia.org/wiki/File:Propermotion.svg> (2018).
URL: <https://commons.wikimedia.org/wiki/File:Propermotion.svg>
- <http://segue.uchicago.edu/> (2007).
URL: <http://segue.uchicago.edu/>
- <http://www.sdss3.org/surveys/> (2013).
URL: <http://www.sdss3.org/surveys/>
- <http://www.sdss3.org/surveys/apogee.php> (2013).
URL: <http://www.sdss3.org/surveys/apogee.php>
- <http://www.sdss3.org/surveys/marvels.php> (2013).
URL: <http://www.sdss3.org/surveys/marvels.php>
- <http://www.sdss.org/background/telescope.html> (2006).
URL: <http://www.sdss.org/background/telescope.html>
- Irrgang, A., Kreuzer, S., Heber, U. and Brown, W. (2018). A quantitative spectral analysis of 14 hypervelocity stars from the mmt survey, *Astronomy & Astrophysics* **615**: L5.

- Irrgang, A., Przybilla, N., Heber, U., Böck, M., Hanke, M., Nieva, M.-F. and Butler, K. (2014). A new method for an objective, χ^2 -based spectroscopic analysis of early-type stars—first results from its application to single and binary b- and late o-type stars, *Astronomy & Astrophysics* **565**: A63.
- Jeffery, C., Hibbert, A. and Behara, N. (2013). Discovery of extremely lead-rich subdwarfs: does heavy metal signal the formation of subdwarf b stars?, *Monthly Notices of the Royal Astronomical Society* **434**(3): 1920–1929.
- Kent, S. M. (1994). Sloan digital sky survey, *Astrophysics and Space Science* **217**(1): 27–30.
- Kupfer, T., Geier, S., Heber, U., Østensen, R., Barlow, B., Maxted, P., Heuser, C., Schaffenroth, V. and Gänsicke, B. (2015). Hot subdwarf binaries from the muchfuss project—analysis of 12 new systems and a study of the short-period binary population, *Astronomy & Astrophysics* **576**: A44.
- Mattig, F. (2022). Bachelor thesis: Radial velocity study of hot subdwarfs.
- Maxted, P., Heber, U., Marsh, T. and North, R. (2001). The binary fraction of extreme horizontal branch stars, *Monthly Notices of the Royal Astronomical Society* **326**(4): 1391–1402.
- Napiwotzki, R. (2008). The origin of helium-rich subdwarf o stars, *In: Hydrogen-Deficient Stars-ASP Conf Series 391*, Astronomical Society of the Pacific.
- Napiwotzki, R., Karl, C., Lisker, T., Heber, U., Christlieb, N., Reimers, D., Nelemans, G. and Homeier, D. (2004). Close binary ehb stars from spy, *Astrophysics and Space Science* **291**(3): 321–328.
- Newell, B. and Graham, J. (1976). Gaps in the blue horizontal branch., *The Astrophysical Journal* **204**: 804–809.
- Newman, P. R., Long, D. C., Snedden, S. A., Kleinman, S., Nitta, A., Harvanek, M., Krzesinski, J., Brewington, H. J., Barentine, J., Neilsen Jr, E. H. et al. (2004). Mass-producing spectra: the sdss spectrographic system, *Ground-based Instrumentation for Astronomy*, Vol. 5492, SPIE, pp. 533–544.
- Popova, E., Tutukov, A. and Yungelson, L. (1982). Study of physical properties of spectroscopic binary stars, *Astrophysics and Space Science* **88**(1): 55–80.
- Saio, H. and Jeffery, C. S. (2000). The evolution of a rapidly accreting helium white dwarf to become a low-luminosity helium star, *Monthly Notices of the Royal Astronomical Society* **313**(4): 671–677.

- Sako, M., Bassett, B., Becker, A., Cinabro, D., DeJongh, F., Depoy, D. L., Dilday, B., Doi, M., Frieman, J. A., Garnavich, P. M. et al. (2007). The sloan digital sky survey-ii supernova survey: search algorithm and follow-up observations, *The Astronomical Journal* **135**(1): 348.
- Smee, S. A., Gunn, J. E., Uomoto, A., Roe, N., Schlegel, D., Rockosi, C. M., Carr, M. A., Leger, F., Dawson, K. S., Olmstead, M. D. et al. (2013). The multi-object, fiber-fed spectrographs for the sloan digital sky survey and the baryon oscillation spectroscopic survey, *The Astronomical Journal* **146**(2): 32.
- The SDSS Instruments* (2005).
URL: <http://cas.sdss.org/dr4/en/sdss/instruments/instruments.asp>
- York, D. G., Adelman, J., Anderson Jr, J. E., Anderson, S. F., Annis, J., Bahcall, N. A., Bakken, J., Barkhouser, R., Bastian, S., Berman, E. et al. (2000). The sloan digital sky survey: Technical summary, *The Astronomical Journal* **120**(3): 1579.
- Zhang, X. and Jeffery, C. S. (2012). Evolutionary models for double helium white dwarf mergers and the formation of helium-rich hot subdwarfs, *Monthly Notices of the Royal Astronomical Society* **419**(1): 452–464.

9 Appendix

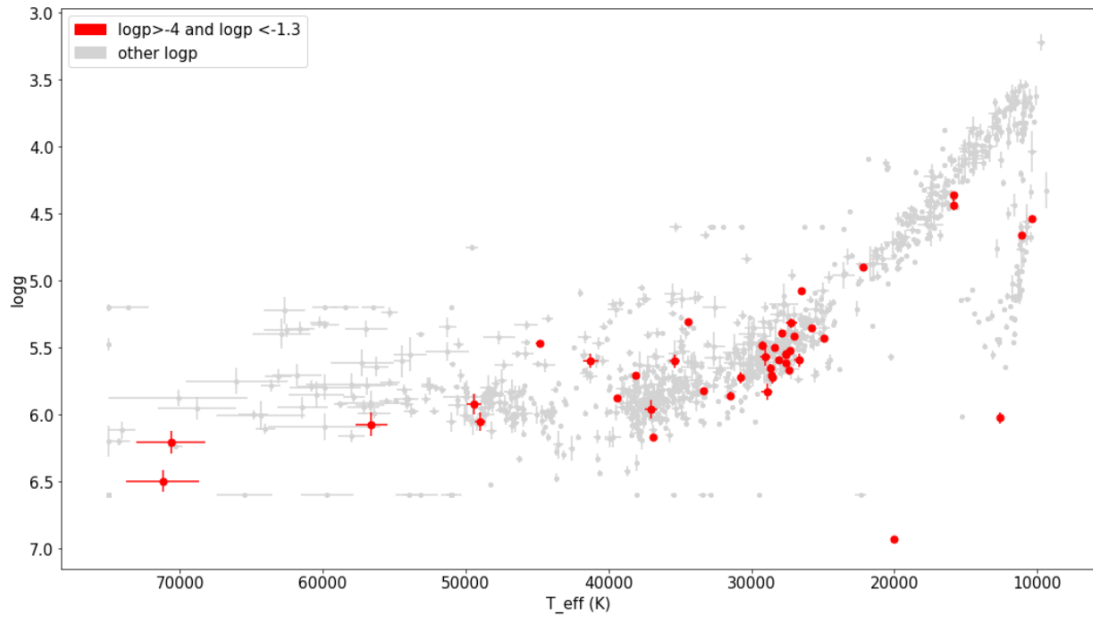


Figure 9.1: Distribution of candidates to be radial velocity variable stars marked in red, where all other types of stars are marked in light grey color.

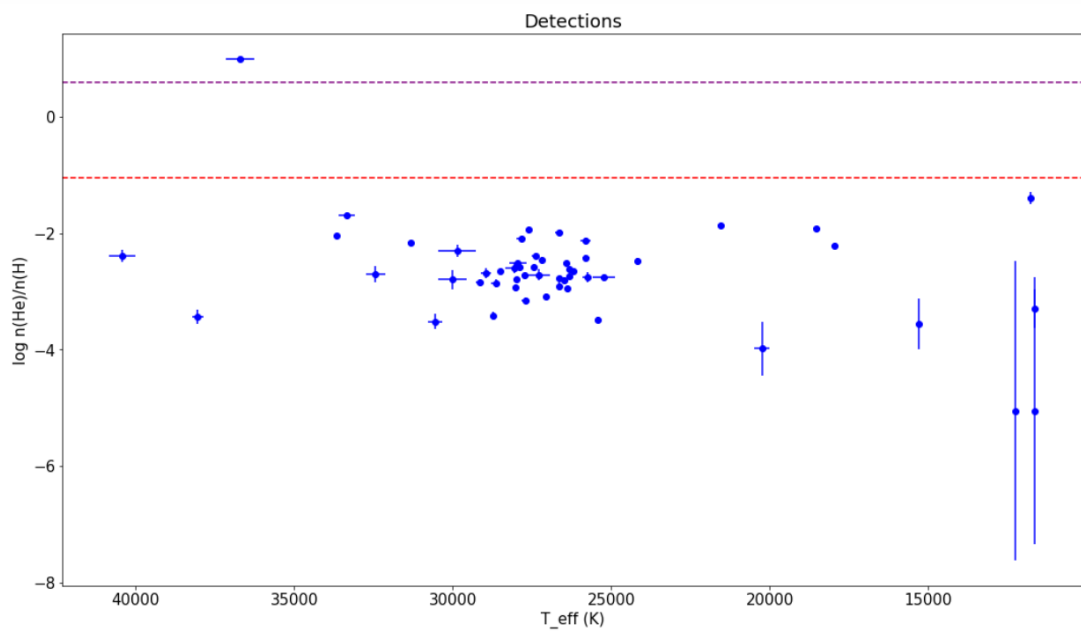


Figure 9.2: Distribution of detected variable subdwarfs by helium abundance. To characterize the different groups of helium abundances, two dashed horizontal lines are inserted. The red one splits the helium poor from the intermediate helium ones and the magenta one splits the group of intermediate helium stars from the group of helium rich stars at solar helium abundances.

Name	$T_{\text{eff}}[K]$	$\log g [\frac{cm}{s^2}]$	$[\log(\frac{nHe}{nH})]$	$\log p$
J180940.41+234328.4	27860 ± 21	5.39 ± 0.002	-3.24 ± 0.13	-3.93
J184434.74+412158.7	27200 ± 450	5.32 ± 0.006	-2.89 ± 0.1	-3.81
J165404.26+303701.8	24960 ± 140	5.425 ± 0.02	-2.77 ± 0.04	-3.70
J191908.76+371423.8	27356 ± 30	5.669 ± 0.005	-2.55 ± 0.06	-3.67
J183349.78+652056.3	25800 ± 240	5.355 ± 0.026	-2.61 ± 0.07	-3.49
J202054.08+135323.4	28900 ± 450	5.83 ± 0.08	-1.83 ± 0.04	-3.48
J183229.21+402418.3	44800 ± 300	5.466 ± 0.025	-2.64 ± 0.06	-3.24
J115358.81+353928.8	28420 ± 75	5.499 ± 0.01	-2.89 ± 0.05	-3.11
J204448.63+153638.7	29060 ± 330	5.56 ± 0.06	-2.54 ± 0.08	-3.10
J091225.13+421922.5	29250 ± 270	5.48 ± 0.04	-5.1 ± 0.6	-2.76
J091432.02+045241.3	12620 ± 180	6.02 ± 0.08	-5 ± 3	-2.71
J124048.60-033708.3	10405 ± 1	4.534 ± 0.02	-5.1 ± 2	-2.59
J093245.91+081618.5	33340 ± 90	5.821 ± 0.01	-1.73 ± 0.02	-2.50
J144709.19+511639.9	49400 ± 550	5.92 ± 0.1	-0.21 ± 0.03	-2.23
J124342.23-032239.9	15860 ± 240	4.43 ± 0.05	-1.82 ± 0.13	-2.19
J151913.31+261720.6	29270 ± 80	5.48 ± 0.01	-3.48 ± 0.13	-2.16
J132357.27+261502.5	26540 ± 110	5.07 ± 0.02	-2.21 ± 0.04	-2.11
J160229.76+111330.9	38140 ± 105	5.70 ± 0.02	-0.678 ± 0.015	-2.09
J165957.60+434136.9	41300 ± 700	5.60 ± 0.07	-2.37 ± 0.14	-2.06
J152046.67+180300.7	36900 ± 170	6.18 ± 0.02	1	-2.03
J125006.63+575122.5	22180 ± 200	4.90 ± 0.026	-2.51 ± 0.1	-2.00
J140747.84+235424.3	39410 ± 130	5.88 ± 0.02	-1.51 ± 0.02	-1.99
J075718.55+440936.9	31460 ± 260	5.861 ± 0.03	-2.5 ± 0.1	-1.99
J030155.43+375434.8	56600 ± 1050	6.1 ± 0.1	-0.037 ± 0.06	-1.94
J053303.89+001459.9	30760 ± 250	5.72 ± 0.06	-3.05 ± 0.19	-1.92
J135831.62+631455.4	49000 ± 450	6.05 ± 0.1	0.59 ± 0.02	-1.77
J094315.81+165557.0	27560 ± 70	5.554 ± 0.01	-2.66 ± 0.04	-1.76
J150829.02+494050.9	28710 ± 210	5.65 ± 0.03	-2.27 ± 0.05	-1.76
J161114.59+032833.0	15890 ± 110	4.36 ± 0.03	-2 ± 0.1	-1.73
J204358.55-065025.8	37000 ± 500	5.96 ± 0.1	-0.072 ± 0.03	-1.72
J114352.74+660723.3	27620 ± 280	5.548 ± 0.03	-2.31 ± 0.07	-1.68
J154728.82+290206.8	20000 ± 5	6.9 ± 0.08	-2.8 ± 0.4	-1.78
J132209.92+401557.3	28630 ± 90	5.71 ± 0.02	-2.64 ± 0.06	-1.51
J125702.30+435245.8	28520 ± 280	5.72 ± 0.1	-3.32 ± 0.2	-1.49
J202519.93+144257.8	26700 ± 450	5.59 ± 0.1	-2.35 ± 0.07	-1.49
J123620.03+283143.8	26990 ± 260	5.42 ± 0.04	-2.62 ± 0.13	-1.44
J010901.74-001112.7	11120 ± 10	4.66 ± 0.003	-1.86 ± 0.05	-1.44
J042106.56+254655.5	27340 ± 120	5.52 ± 0.02	-2.34 ± 0.02	-1.41
J204546.81-054355.7	35400 ± 500	5.6 ± 0.1	-1.8 ± 0.1	-1.40
J225638.34+065651.0	28120 ± 140	5.59 ± 0.02	-2.81 ± 0.05	-1.36

J145426.67+472004.3	27590 ± 50	5.61 ± 0.005	-2.46 ± 0.022	-1.34
J173027.20+265639.5	70600 ± 2400	6.2 ± 0.1	1 ± 0.04	-1.32
J120613.39+205523.1	34400 ± 170	5.31 ± 0.02	-2.43 ± 0.05	-1.31
J112457.67+153426.6	71200 ± 2400	6.5 ± 0.09	-1.36 ± 0.1	-1.31

Table 7: Candidates for RV variability. The name of the star and the determined p value is given, as well as the atmospheric parameters T_{eff} , $\log g$ and the helium to hydrogen abundance ratio $\log \frac{n(\text{He})}{n(\text{H})}$.

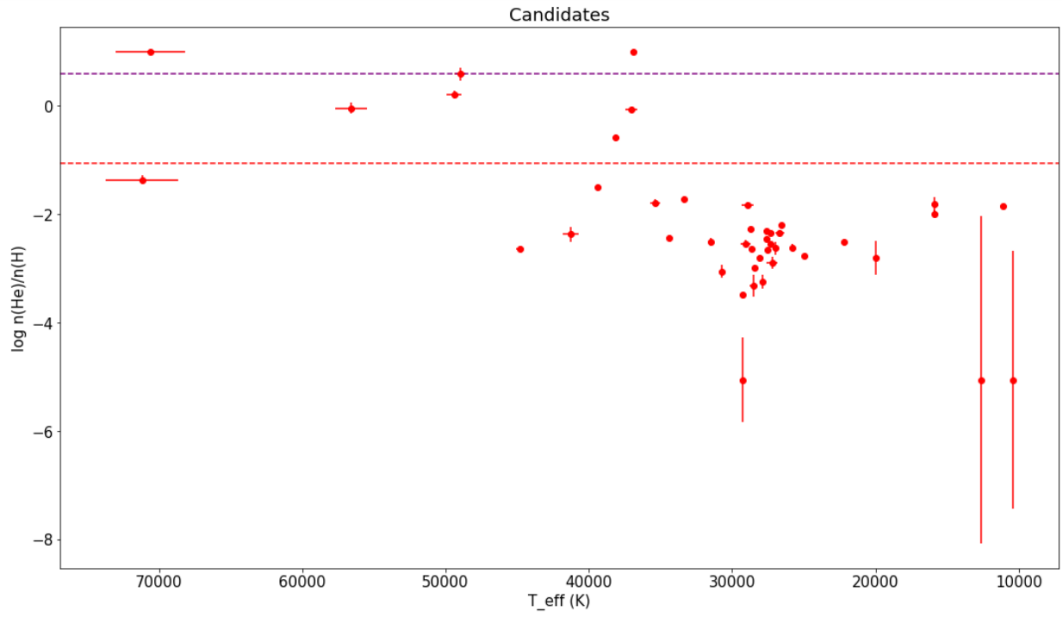


Figure 9.3: Distribution of candidates for variable subdwarfs by helium abundance. To characterize the different groups of helium abundances, two dashed horizontal lines are inserted. The red one splits the helium poor from the intermediate helium ones and the magenta one splits the group of intermediate helium stars from the group of helium rich stars.

Name	$T_{\text{eff}} [K]$	$\log g \left[\frac{\text{cm}^2}{\text{s}^2} \right]$	$\log \left(\frac{n_{\text{He}}}{n_{\text{H}}} \right)$	$\log p$	period[d]	Identifier
J140118.80-081722.6	15290 ± 54	6.016 ± 0.007	-3.6 ± 0.9	-252.07	2.71	(5)
J075610.71+670424.6	11780 ± 105	5.12 ± 0.05	-1.39 ± 0.01	-101.6	-	(1)
J134632.65+281722.7	26377 ± 24	5.319 ± 0.006	-2.95 ± 0.014	-78.03	-	(1)
J083006.17+475150.4	25444 ± 3.5	5.469 ± 0.0041	-3.48 ± 0.04	-69.77	0.148	(2)
J211651.96-003328.4	26640 ± 120	5.415 ± 0.001	-2.91 ± 0.06	-58.63	-	(1)
J151733.34+225908.0	26330 ± 70	5.430 ± 0.011	-2.55 ± 0.04	-55.49	-	(1)
J095101.28+034757.0	27990 ± 65	5.556 ± 0.01	-2.76 ± 0.04	-44.46	0.42	(2)
J012022.94+395059.4	27720 ± 115	5.391 ± 0.019	-3.14 ± 0.06	-19.06	-	(3)
J162256.66+473051.1	27619 ± 49	5.649 ± 0.001	-1.63 ± 0.012	-14.27	0.069	(3)
J092520.69+470330.6	27910 ± 105	5.512 ± 0.017	-2.53 ± 0.07	-14.09	-	(3)
J183249.04+630910.7	26200 ± 130	5.287 ± 0.025	-2.63 ± 0.04	-13.67	-	(2)
J164326.04+330113.1	27950 ± 235	5.61 ± 0.04	-2.50 ± 0.04	-12.54	-	(3)
J082053.53+000843.4	25820 ± 135	5.452 ± 0.016	-2.10 ± 0.016	-9.15	-	(4)
J152222.14-013018.3	25240 ± 320	5.388 ± 0.026	-2.74 ± 0.07	-7.53	-	(3)
J192059.77+372220.0	27400 ± 110	5.456 ± 0.019	-2.38 ± 0.02	-5.39	-	(2)
J204613.40-045418.7	30550 ± 225	5.54 ± 0.04	-3.52 ± 0.27	-4.06	-	(3)

Table 8: Radial velocity variable objects, which were identified as RV variables before are listed in this table. The atmospheric parameters of T_{eff} , $\log g$ and helium to hydrogen abundance ratio $\log \left(\frac{n_{\text{He}}}{n_{\text{H}}} \right)$ are also given as well as the determined $\log p$ value and the paper in which those stars were detected as variables. (1) is the paper of Geier et al. (2022), (2): (Kupfer et al.; 2015), (3): (Geier et al.; 2011b), (4): (Geier et al.; 2011a), (5): (El-Badry et al.; 2021).

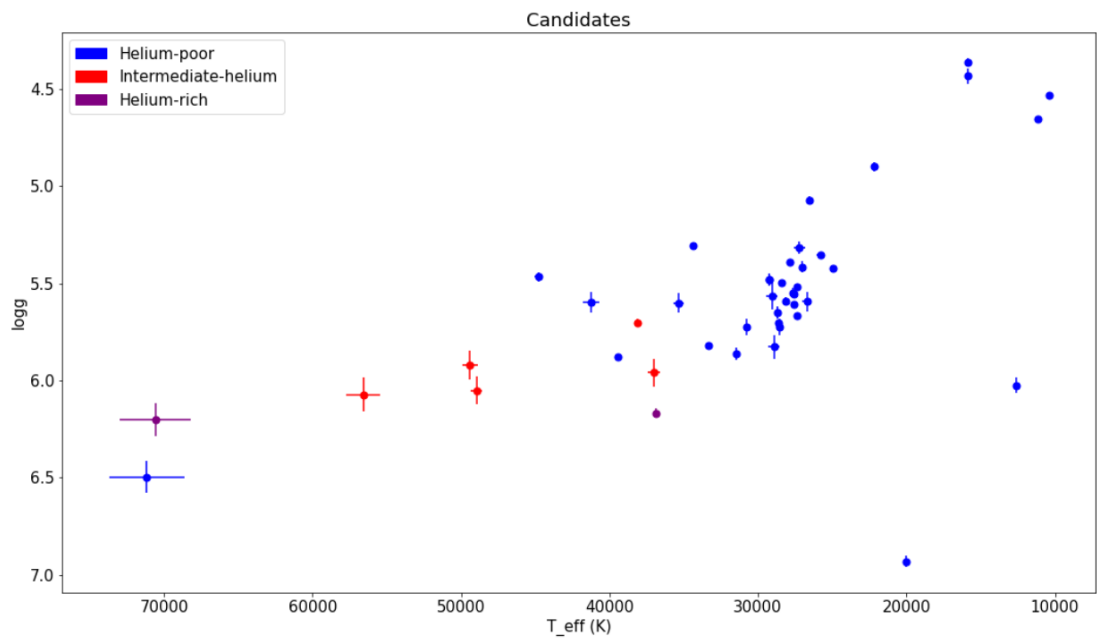


Figure 9.4: Candidates for RV variability in the Kiel-diagram. The different helium abundances are indicated by different colors.

Name	T_{eff} [K]	$\log g$
J152046.67+180300.7	36900 \pm 170	6.18 \pm 0.02
J161624.35+265314.8	40640 \pm 130	6.44 \pm 0.035
J121029.23+090553.9	43830 \pm 125	5.98 \pm 0,02
J153701.00+182024.4	40800 \pm 240	6.16 \pm 0.04
J094856.95+334150.9	50010 \pm 450	5.8 \pm 0.015
J204055.91+140037.5	40070 \pm 220	6.58 \pm 0.014
J081304.04-071306.4	48130 \pm 360	5.91 \pm 0.073
J152708.31+003308.3	40760 \pm 240	6.33 \pm 0.025
J151030.68-014345.9	44520 \pm 270	5.99 \pm 0.19
J163027.19+180233.2	47080 \pm 380	5.98 \pm 0.17
J132856.71+310846.0	75000 \pm 1200	6.20 \pm 0.035
J131218.11+381535.1	38700 \pm 250	6.42 \pm 0.018
J133202.60+523734.9	43520 \pm 245	6.22 \pm 0.057
J001837.14+152149.9	43620 \pm 430	6.47 \pm 0.038
J161740.10+411251.6	38000 \pm 245	6.03 \pm 0.075
J164042.90+311734.6	39710 \pm 465	6.17 \pm 0.028
J200550.04+762536.3	43090 \pm 375	5.90 \pm 0.048
J154043.09+435950.1	45480 \pm 455	5.87 \pm 0.032
J084125.44+610320.6	44200 \pm 390	5.97 \pm 0.019
J160233.32+361345.3	45950 \pm 290	6.00 \pm 0.029
J153056.33+024222.5	46060 \pm 330	5.83 \pm 0.023
J001908.55+242422.3	38420 \pm 195	5.96 \pm 0.022
J114604.92+082934.9	46270 \pm 235	5.83 \pm 0.012
J163702.79-011351.7	46300 \pm 325	5.85 \pm 0.019
J034822.28+113303.3	43960 \pm 330	5.95 \pm 0.020
J142700.08+584700.7	43140 \pm 325	6.30 \pm 0.041
J141549.05+111213.8	43000 \pm 480	5.92 \pm 0.022
J180757.07+230133.0	42160 \pm 310	6.16 \pm 0.011
J164634.49+263752.3	37990 \pm 185	6.01 \pm 0.047
J153526.07+211440.9	38310 \pm 195	6.10 \pm 0.024
J215553.90+202802.9	46460 \pm 300	6.01 \pm 0.022
J171703.15+271637.0	37860 \pm 155	6.16 \pm 0.039
J162435.66+150355.4	45950 \pm 445	6.14 \pm 0.039
J161345.80+384950.9	44040 \pm 460	5.91 \pm 0.016
J141505.47+020237.0	44060 \pm 465	6.02 \pm 0.030
J132747.87+564040.0	48380 \pm 300	5.95 \pm 0.024
J134226.52+290343.4	43630 \pm 330	6.27 \pm 0.019
J204940.86+165003.6	44680 \pm 450	6.05 \pm 0.048
J133543.00+330558.4	44650 \pm 440	5.98 \pm 0.036

J151415.66-012925.2	48690 ± 455	5.89 ± 0.022
J173027.20+265639.5	70600 ± 330	6.20 ± 0.1
J155155.11+092344.0	44370 ± 225	6.00 ± 0.030
J123808.65+053318.2	48250 ± 465	5.91 ± 0.027
J143006.23+510314.0	45940 ± 550	5.82 ± 0.018
J072726.40+444837.0	48740 ± 480	5.86 ± 0.033
J161627.10-002932.9	46410 ± 440	5.94 ± 0.055
J102241.21+203839.6	41980 ± 280	5.09 ± 0.048
J162654.19+082534.9	43380 ± 230	6.08 ± 0.035
J203426.11+141715.0	38010 ± 215	6.36 ± 0.074
J085351.77+070417.3	45910 ± 530	6.03 ± 0.026
J161507.08+105513.5	47570 ± 535	5.96 ± 0.044
J083747.23+194955.8	48190 ± 650	6.12 ± 0.056
J155729.93+485023.2	44450 ± 235	6.09 ± 0.035
J112414.45+402637.1	48600 ± 555	6.00 ± 0.037
J151628.36+340657.6	48430 ± 625	5.83 ± 0.017
J104739.10+094424.1	44600 ± 590	6.13 ± 0.022
J103806.65+134412.0	48050 ± 460	5.83 ± 0.024
J023532.60-063437.8	44220 ± 370	6.17 ± 0.042
J160932.41+223749.8	45200 ± 620	5.91 ± 0.122
J224739.95+071732.5	47470 ± 370	5.74 ± 0.033
J152143.87+450022.5	43480 ± 725	5.77 ± 0.038
J200836.41-114629.2	46910 ± 690	5.84 ± 0.029
J155550.39+403853.9	39290 ± 380	5.89 ± 0.033
J200815.48-110103.9	48310 ± 475	5.97 ± 0.040

Table 9: List of all stars, where the fit ended up at the upper border for helium abundance of the standard grids ($\log \frac{n(\text{He})}{n(\text{H})} = 1$)

Acknowledgements

I would like to thank my research supervisor Uli Heber for this opportunity to work at the observatory and introducing me to the highly interesting topic hot subdwarfs. I was able to expand my knowledge and immerse myself in a fascinating field of astronomy.

I also want to express special thanks to Matti Dorsch, who helped me with any technical issue, wherever he can, especially for problems with the Python codes. I also want to thank Aakash Bhat and Sebastian Weich, as well as Matti and Uli for the nice, interesting and revealing discussions in our weekly meetings.

Furthermore I want to thank Manami Sasaki to take the second opinion in the evaluation of this thesis.

I am grateful to everyone at the Remeis observatory I had the pleasure to meet and talk with.

Eidesstattliche Erklärung

Ich erkläre hiermit, dass ich die vorliegende Arbeit selbständig verfasst, andere als die angegebenen Quellen/Hilfsmittel nicht benutzt, und die den benutzten Quellen wörtlich und inhaltlich entnommenen Stellen als solche kenntlich gemacht habe.

Höchstadt, am 04.01.2023

.....
Philipp Jeßberger